Computational Studies of Peptide Self-Assembly

By

KASSANDRA L. SCHMIDT

A thesis submitted to the

School of Graduate Studies

Rutgers, The State University of New Jersey

In partial fulfillment of the requirements

For the degree of

Master of Science

Graduate Program in Biomedical Engineering

Written under the direction of

Meenkashi Dutt

And approved by

____

____

____

New Brunswick, New Jersey

October 2019

ABSTRACT OF THE THESIS

Computational Studies of Peptide Self-Assembly

by KASSANDRA SCHMIDT

Thesis Director:

Dr. Meenakshi Dutt

Research into novel biological materials for use in biomedical applications is guided by the formation of supramolecular structures which have properties resultant from the characteristics of the compositional molecules. Peptides are commonly utilized in biological material development as their properties are widely variable and highly controllable due to the sequence-specific properties of amino acids. Self-assembling peptides are of specific interest due to their spontaneous aggregation into organized morphologies with predictable characteristics based upon their constituent amino acids. Though novel peptide materials have traditionally been researched through physical experimentation, the development of Molecular Dynamics has allowed for comparable computational studies of peptide systems. In this work, coarse-grained Molecular Dynamics simulations are selected to study self-assembling peptides from two classes, aromatic and aliphatic, as these peptides have been experimentally validated to spontaneously assemble themselves into nanostructures. Computational models representative of the peptides' chemistry are created for aromatic peptides FF (phenylalanine-phenylalanine) and FNF (phenylalanine-asparagine-phenylalanine) and aliphatic peptides A_6K (alanine-alanine-alanine-alanine-alanine-alanine-lysine), V_6K (valine-valine-valine-valine-valine-valine-lysine), and V_6K_2 (valine-valine-valine-valine-

valine-valine-lysine-lysine). In the aromatic studies, the effect of varying total peptide concentrations and relative tripeptide concentrations on the morphology of the assembled structures is characterized. In the aliphatic studies, the peptide alignment in stable aggregates and nanostructures is determined. The results demonstrate the viability of these peptide systems to form stable, usable nanostructures suitable for inclusion in biological applications that require the respective specific properties of the in-scope peptides.

Acknowledgements

First and foremost, I would like to whole-heartedly thank my research advisor, Dr. Meenakshi Dutt, for the many opportunities she has afforded me during my time at Rutgers University. I entered Rutgers as an engineer with little research experience and working in the Computational Hybrid Soft Materials Laboratory has allowed me to develop and cultivate the tools and mindset of a scientist. Dr. Dutt has always encouraged me to grow through my work, to strive for higher and higher self-standards. Her vested interest in my professional development and unconditional support has been instrumental in enabling me to expand the reach of my potential, to truly advocate for myself, and to envision what additional opportunities I might pursue in the future.

I would like to extend sincere thanks to my thesis defense committee members, Dr. Vikas Nanda and Dr. Wilma Olson, for the generous sharing of their time and knowledge. I have collaborated with Dr. Nanda on a paper (doi:10.1039/c8ob00130h). He is an inspired scientist who has greatly helped the progression of my research. Dr. Olson is roundly regarded as an expert in her work, and I am grateful that she has agreed to help me in the advancement of my thesis.

My experience in Dr. Dutt's Computational Hybrid Soft Materials Laboratory would have been markedly less enriching and gratifying without the companionship and guidance of my learned colleagues. First, I would like to express gratitude to Srinivas Mushnoori for taking on the additional responsibility of being my mentor and teaching me about performing computational research. He has always made himself available if I have encountered problems, had questions, or required his collaboration to ensure the best possible outcomes. I would like to thank Akash Banerjee for his friendship and his support.

Having entered the research group together, it has been a formative experience to learn and work beside him. I would also like to thank Yu Chien Lu for his collaborative and dedicated nature. Yu Chien, who works on a project parallel to one of mine, has been a valuable resource in the development and progression of my work. Lastly, I would like to acknowledge Daniel Grisham and Tianyou Mou for their valuable insights on the aromatic peptide study.

I would like to acknowledge the Extreme Science and Engineering Discovery Environment (XSEDE) [allocation TG-DMR140125] for access to the computational resources which have made my research possible. Specifically, I would like to thank the San Diego Supercomputer Center (SDSC) and the Texas Advanced Computing Center (TACC) for the use of their systems to perform research. I would like to thank and acknowledge Dr. Haim Baruh and the New Jersey Space Grant Consortium (NJSGC) [grant number NNX15AK05H] for their financial support during this crucial phase of my educational journey.

In terms of professional development, I would like to thank Dr. Masanori Hara for the opportunity to mentor visiting undergraduate NSF scholars through the Research Intensive Summer Experience (RiSE) program [PI of NSF REU on Advanced Materials], and Emran Reshid for working with me on projects that have continued to benefit the research group after the program ended. I would like to also thank Dr. Martha Soto for the opportunity to be a mentor to high school sophomores through the BIOsciences Links to Teaching Program (BIOLinks). I am grateful to Ms. Rebecca Donatelli, a chemistry teacher at New Brunswick High School, for her guidance, support, and willingness to share her experiences and coach me in order to make me a better mentor now and in future capacities.

I would like to thank the Rutgers Office of Research Commercialization (ORC) for the opportunity to intern under professional licensing managers. I would like to specifically acknowledge Andrea Dick and Dan Benderly, who expanded my knowledge about technology transfer outside of my formal training, provided me numerous diverse learning opportunities, and enabled me to contribute to the success of their department.

Lastly, I would like to thank my parents. They have encouraged my academic pursuits my entire life, and it is thanks to their encouragement and support that I have been able to succeed and accomplish all of my goals.

Table of Contents

ABSTRACT OF THE THESIS …………………………………………………………. ii

Acknowledgements ……………………………………………………………….. iv

Table of Contents ………………………………………………………………… vii

List of Figures ……………………………………………………………………... ix

List of Tables ……………………………………………………………………... xiii

Chapter 1: An Introduction to the Work ………………………………………………. 1

Chapter 2: Molecular Dynamics Simulations and Peptide Coarse-Grained Modeling ….. 3

2.1 Simulation Framework for Computational Investigation ………………... 3

2.2 Mathematical Interactions ……………………………………………….. 5

2.2.1 Non-Bonded Interactions ………………………………………... 5

2.2.2 Bonded Interactions ……………………………………………... 6

2.3 Coarse-Grained Parameterization Based on Particle Types ……………... 9

2.3.1 Amino Acid Mapping …………………………………………… 9

2.3.2 Water Mapping ………………………………………………… 11

2.3.3 Ion Mapping …………………………………………………… 13

2.4 Time Scale Interpretation ……………………………………………….. 13

Chapter 3: Hybrid Aromatic Ultra-Short Peptide System ……………………………… 14

3.1 Overview of Diphenylalanine and Molecular Composition ……………...14

3.2 Model Parameterization and Computational Methods ………………….. 15

3.2.1 Topology Design ……………………………………………….. 15

3.2.2 Simulation Parameters ………………………………………….. 16

3.3 Simulation Results of 55 Unique Molecular Compositions …………….. 17

3.3.1 Morphological Variation Quantified ……………………………. 17

3.3.2 Assembly Pathways …………………………………………….. 22

3.3.3 Influence of the Tripeptide on Nanostructure Formation ……….. 25

3.4 Conclusions of the Aromatic Peptide Study …………………………….. 28

Chapter 4: Aliphatic Peptide Model Design …………………………………………….. 29

4.1 General Overview of A_6K and V_6K ………………………………..….. 29

4.2 Model Parameterization and Computational Methods …………………. 30

4.2.1 Topology Design ……………………………………………….. 30

4.2.2 Simulation Parameters – A_6K and V_6K …………………………. 34

4.2.3 Simulation Parameters – V_6K_2 ……………..…………………… 35

4.3 A_6K and V_6K Model Validation ……………………………………..... 37

4.4 V_6K_2 Model Validation ……………………………………………….… 40

4.4.1 Nanostructure Comparison …………………………………... 40

4.4.2 Influence of Water Model on Nanostructure Organization ……... 41

4.5 Conclusions of the Aliphatic Peptide Study ……………………..…… 43

Chapter 5: Future Directions ………………………………………………………. 45

Bibliography

List of Figures

Figure 2.1. Coarse-grained representation of the twenty natural amino acids. The beads are color-coded by their interaction site type. Reprinted with permission from L. Monticelli, S. K. Kandasamy, X. Periole, R. G. Larson, D. P. Tieleman and S.-J. Marrink, *Journal of Chemical Theory and Computation*, 2008, **4**, 819–834. Copyright © 2007, American Chemical Society ..…………………….....…………………………………………. 4

Figure 2.2. A comparison of MARTINI standard water (A) and MARTINI polarizable water (B). The orange sphere is the van der Waals radii of particle W. (Yesylevskyy SO, Schäfer LV, Sengupta D, Marrink SJ (2010) Polarizable Water Model for the Coarse-Grained MARTINI Force Field. PLoS Comput Biol 6(6): e1000810. https://doi.org/10.1371/journal.pcbi.1000810. Copyright: © 2010 Yesylevskyy et al.) ... 12

Figure 3.1. Coarse-grained representations of (a) diphenylalanine (FF) and (b) phenylalanine-asparagine-phenylalanine (FNF). The left-most picture shows the MARTINI approximation over an AA model of the peptides. The middle picture details the MARTINI particle types assigned to each approximation, and the last picture shows the MARTINI representation of the peptide.……………………………………………..16

Figure 3.2 Representative pictures of each of the four hybrid nanostructures formed in the phase space: (a) lamellar bilayer, (b) axial cross-sectional view of a nanotube, (c) diametrical cross-sectional view of a vesicle, and (d) disordered assembly…………….. 18

Figure 3.3. Histogram of the occurrence of vesicles in the phase space for different molecular compositions. These measurements used 10 independent particle trajectories for each molecular composition……………………………………………………….. 20

Figure 3.4. Histogram of the occurrence of lamellar bilayers in the phase space for different molecular compositions. These measurements used 10 independent particle trajectories for each molecular composition……………………………………………………………….. 21

Figure 3.5. Histogram of the occurrence of nanotubes in the phase space for different molecular compositions. These measurements used 10 independent particle trajectories for each molecular composition……………………………………………………………….. 22

Figure 3.6. Histogram of the occurrence of disordered nanostructures in the phase space for different molecular compositions. These measurements used 10 independent particle trajectories for each molecular composition…………………………………………….. 22

Figure 3.7. The assembly pathways reported in other works that are represented in this study's computational work. (a) At low total peptide concentrations, smaller vesicles fused to make larger ones. (b) At higher relative tripeptide concentrations, the peptides assembled into a bilayer which then folded into a nanotube…………………………………….... 23

Figure 3.8. Phase space map of the four morphologies found at each total peptide concentration and each relative tripeptide concentration. The most representative structure of the ten simulations for that molecular composition is presented; if more than one structure was equally represented, all of those morphologies are presented……………….. 24

Figure 3.9. The pinching effect caused by the inclusion of FNF in an FF bilayer. The yellow arrows represent the hydrophobic attraction between the phenylalanine side chains, the red arrows represent the hydrophilic interactions between the peptide backbones, the asparagine side chains, and the solvent particles, and the purple arrows indicate electrostatic attractions……………………………………………………………………….. 25

Figure 3.10. Distribution of the angle of the FNF backbone beads. The average angle is 112.9°, which is higher than the equilibrium angle of FNF at 107.4°…………………..... 26

Figure 3.11. Density of FNF tripeptides plotted against the z-axis coordinate for the total peptide concentration 0.3 peptides/nm^3 and the relative tripeptide concentration 50%. Traveling through the lamellar bilayer results in two closely spaced peaks, indicating that the tripeptides are evenly distributed on the top and bottom of the lamellar bilayer……. 27

Figure 4.1. A summary of secondary structure propensity in A_6K and V_6K. (a) The average propensity of each detected secondary structure over the middle five residues of each peptide. (b) The propensity of the coil secondary structure in A_6K and V_6K. (c) The propensity of the β-sheet secondary structure in A_6K and V_6K. A_6K prefers to adapt a coil secondary structure, and V_6K prefers to adapt a β-sheet secondary structure. (Reprinted with permission from Y. Sun, Z. Qian, C. Guo and G. Wei, *Biomacromolecules*, 2015, **16**, 2940–2949. Copyright © 2015, American Chemical Society.)……………………….… 32

Figure 4.2. Coarse-grained representations of (a) A_6K (b) V_6K………………………… 33

Figure 4.3. An AA representation, a CG ideal, and the MARTINI CG representations of the developed topologies for A_6K (a), (c), (e) and V_6K (b), (d), (f). (a) and (b): (Reproduced from Ref. 67 with permission from The Royal Society of Chemistry). (c) and (d): (Reprinted with permission from Y. Sun, Z. Qian, C. Guo and G. Wei, *Biomacromolecules*, 2015, **16**, 2940–2949. Copyright © 2015, American Chemical Society.) ………...…………………………………………………………...…………………..33

Figure 4.4. The MARTINI CG representations of the developed topologies for (a) A_6K_2, (b) V_6K_2, and (c) V_6K_3. ………………………………………………………………… 34

Figure 4.5. Final assembles from three different views for (a) A_6K and (b) V_6K. Alanine, valine, and lysine backbone beads are in pink, valine side chain beads are in yellow, and lysine side chain beads are in blue. (Reprinted with permission from Y. Sun, Z. Qian, C. Guo and G. Wei, *Biomacromolecules*, 2015, **16**, 2940–2949. Copyright © 2015, American Chemical Society.) …………………………………………………………………… 38

Figure 4.6. The final assemblies of the developed topologies for (a) A_6K and (b) V_6K. The pictures are colored based upon Figure 4.2 …..………………………………………… 39

Figure 4.7. The final assemblies of the developed topologies for (a) A_6K and (b) V_6K. from three different angles, color-coded to match Figure 4.5 …………………………... 39

Figure 4.8. Self-assembled V_6K_2 nanorod parameterized by the developed topology. The nanorod stabilizes itself by interacting with itself through periodic boundaries. The colors are the same as those in Figure 4.2. …………………………………………………. 40

Figure 4.9. Self-assembled V_6K_2 nanorod parameterized by the developed topology. The nanorod stabilizes itself by interacting with itself through periodic boundaries. This nanorod was produced with standard water. The colors are the same as those in Figure 4.2. ……………………………………………………………………………………...… 42

Figure 4.10. Comparison of the two V_6K_2 self-assembled nanorods formed by (a) polarizable water and (b) standard water. Both nanorods are have different dimensions and the peptides pack differently. The colors are the same as those in Figure 4.2………..…. 43

List of Tables

Table 2.1. Backbone bonded parameters for each of the different secondary structures supported by the MARTINI force field. Reprinted with permission from L. Monticelli, S. K. Kandasamy, X. Periole, R. G. Larson, D. P. Tieleman and S.-J. Marrink, *Journal of Chemical Theory and Computation*, 2008, **4**, 819–834. Copyright © 2007, American Chemical Society ………………………………………………………………………… 7

Table 2.2. Equilibrium angles, improper dihedral angles, and the corresponding force constants for each categorized by amino acid. The amino acids who force constants are not specified are categorized as constraints in the topology file. Reprinted with permission from L. Monticelli, S. K. Kandasamy, X. Periole, R. G. Larson, D. P. Tieleman and S.-J. Marrink, *Journal of Chemical Theory and Computation*, 2008, **4**, 819–834. Copyright © 2007, American Chemical Society ……………………………………………………….. 8

Table 2.3. Bond lengths and corresponding force constants for amino acids with side chains. The amino acids who force constants are not specified are categorized as constraints in the topology file. (Reprinted with permission from L. Monticelli, S. K. Kandasamy, X. Periole, R. G. Larson, D. P. Tieleman and S.-J. Marrink, *Journal of Chemical Theory and Computation*, 2008, **4**, 819–834. Copyright © 2007, American Chemical Society) ...…... 8

Table 2.4. Backbone particle types based upon different kinds of secondary structure. What the characterization implies about the particle is specified in Section 2.1. Reprinted with permission from L. Monticelli, S. K. Kandasamy, X. Periole, R. G. Larson, D. P. Tieleman and S.-J. Marrink, *Journal of Chemical Theory and Computation*, 2008, **4**, 819–834. Copyright © 2007, American Chemical Society ……………………………………… 9

Table 2.5. Side chain particle types based upon different kinds of secondary structure. What the characterization implies about the particle is specified in Section 2.1. Reprinted with permission from L. Monticelli, S. K. Kandasamy, X. Periole, R. G. Larson, D. P. Tieleman and S.-J. Marrink, *Journal of Chemical Theory and Computation*, 2008, **4**, 819–834. Copyright © 2007, American Chemical Society ……………………………………... 10

Table 3.1 Summary of the four morphologies formed across the five total peptide concentrations and eleven relative tripeptide concentrations…………………………… 19

Table 3.2. Distribution of FNF on either side of a bilayer for the three different organized morphologies. The total peptide concentration is 0.25 peptides/nm^3 and the relative tripeptide concentration is 10% 27

Chapter 1

An Introduction to the Work

The spontaneous assembly of biological molecules such as peptides/proteins, lipids, and nucleic acids into organized structures has become an increasingly popular component in the development of novel biological materials. Extensive research has been dedicated to the study and determination of natural building blocks which, when combined together, will produce a biological material with desired characteristics. Specifically, materials created from self-assembling peptides have been of interest due to their biocompatibility, controlled variability, and application versatility. Peptides are naturally occurring molecules whose compositions can be varied through the addition or deletion of any of the twenty amino acids in the sequence. A high degree of control can be imposed on a biological material due to the ability to specify peptide sequences, which is especially important when engineering materials for the medical field.

Self-assembling peptides have been used in a multitude of applications in the medical and technological fields. Peptides have been used in the study of neurodegenerative diseases[1-3] and cancer[4-6], drug development and delivery[7-10], gene delivery[11-12], 3D cell culturing[13-18], regenerative medicine[19-21], membrane protein stabilization[22-24], and anti-microbial agents[25-27]. Such a broad range of applications is possible due to the diversity of structures into which self-assembling peptides can aggregate. The work presented in the upcoming chapters accomplishes the following goals: development of computational models for experimentally well-studied peptides within a specific framework, characterization of assemblies formed by peptide aggregation, validation of experimental results, and explanation of peptide self-assembly mechanisms.

In Chapter 2, Molecular Dynamics (MD) simulations are introduced as a tool for computationally studying particle systems and it is explained why coarse-grained (CG) modeling was chosen to develop all of the peptide systems studied. The development of CG peptide models for use with the MARTINI CG force field is detailed as well as the parameters of the force field itself.

In Chapter 3, CG models of diphenylalanine (FF) and phenylalanine-asparagine-phenylalanine (FNF) are created for use within the MARTINI framework. 550 systems comprised of mixtures of the two aromatic peptides are created by varying both the total peptide concentration (the number of peptides per unit volume) as well as the relative tripeptide concentration (the percentage of the total number of peptides which are FNF). The resultant phase space of these simulations is then characterized. The effect FNF has on assembly pathway of FF as well as on the local curvature it induces in an FF bilayer is explored.

In Chapter 4, CG models of amphiphilic peptides A_6K, V_6K, and some of their derivatives are created for use within the MARTINI framework. The validation of A_6K and V_6K against existing computational studies is performed, and a derivative of V_6K (V_6K_2) is validated via comparison with experimental studies. The influence of two of the water models used with the MARTINI framework on the self-assembled nanorods produced by V_6K_2 is investigated.

In Chapter 5, potential future directions for the reported peptide self-assembly projects are presented.

Chapter 2

Molecular Dynamics Simulations and Peptide Coarse-Grained Modeling

2.1 Simulation Framework for Computational Investigation

Molecular Dynamic (MD) simulations allow for the computational investigation of particle interactions as they evolve. By integrating Newton's equations of motion over time, MD simulations can provide insight into the properties of a particle system as it develops and progresses. MD simulations can reveal many details to both support and expand on experimental work with minimal parameters and an initial trajectory. However, these details come with a cost: the higher the requested accuracy, the higher the computational cost of the simulation. When working with systems at the nano- and micro-scale level, all-atom (AA) simulations provide a high level of chemical detail but are computationally expensive and therefore cannot be run over large timescales. Coarse-grained (CG) models sacrifice detail for significantly less computational expense, with modeling efficiently performed over longer temporal scales. When studying small-scale peptides, the benefit of the atomistic detail provided by AA simulations is outweighed by the limitations on simulation run time imposed by relatively high computational costs. Thus, CG MD simulations provide a valuable balance between accuracy and efficiency when studying the effective chemical characteristics of a system.

For simulating biological systems in the CG framework, the MARTINI Force Field: Coarse-Grained Model for Biomolecular Simulations[28] has an excellent track record for providing accurate representations of modeled physical systems. The MARTINI Force

Field was originally developed to simulate lipid systems, but extensions into carbohydrates[29], nucleic acids[30, 31], and peptides and proteins[32] have expanded the uses of the force field. For these reasons, the MARTINI framework was chosen for this research. The model uses a four-to-one mapping (i.e., on average, four heavy atoms and their associated hydrogens are represented by a single interaction center (bead)) though exceptions are made for ring-like molecules, which use a higher resolution mapping for better accuracy. Four main types of interaction sites are used to represent the underlying nature of the beads: apolar [C], non-polar [N], polar [P], and charged [Q]. Each main type has subtypes, which are categorized by hydrogen-bonding capabilities (donor [d], acceptor [a], both [da], or none [0]) and the degree of polarity (lower polarity [1] to higher polarity [5]). Figure 2.1[32] shows the coarse-grained representation of all the natural amino acids based upon the MARTINI classification.

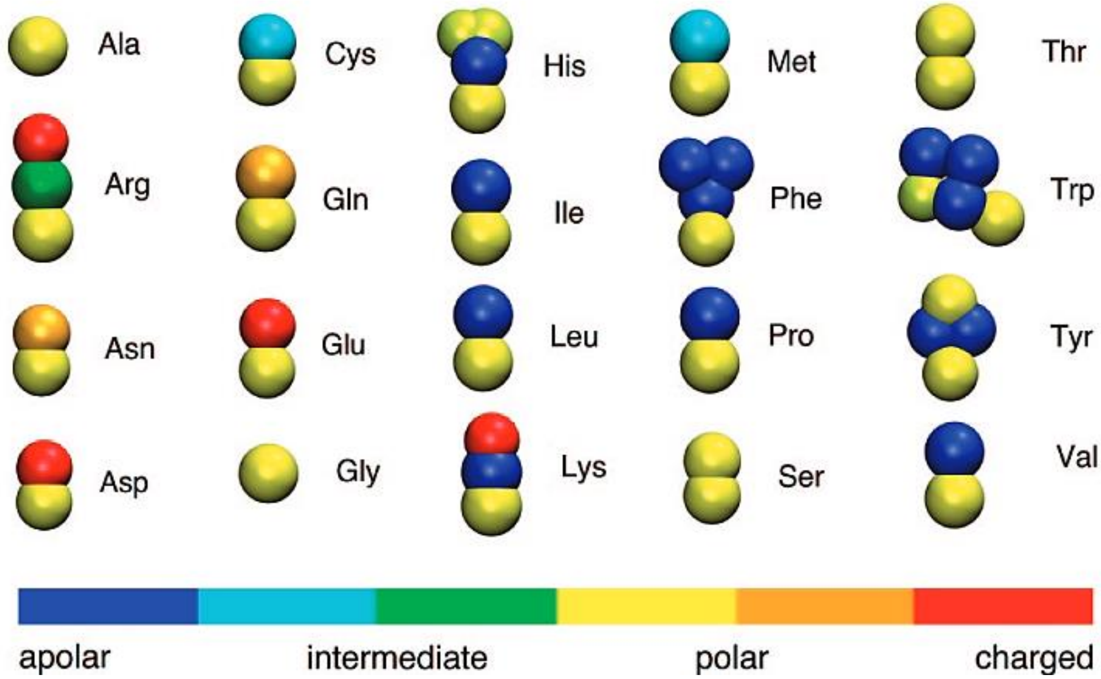

Figure 2.1. Coarse-grained representation of the twenty natural amino acids. The beads are color-coded by their interaction site type. (Reprinted with permission from L. Monticelli, S. K. Kandasamy, X. Periole, R. G. Larson, D. P. Tieleman and S.-J. Marrink, *Journal of Chemical Theory and Computation*, 2008, **4**, 819–834. Copyright © 2007, American Chemical Society.)

2.2 Mathematical Interactions

The particle interactions in the MARTINI CG force field can be classified into two categories: non-bonded and bonded interactions. The MARTINI model uses simple, analytical functions to capture these interactions.

2.2.1 Non-Bonded Interactions

All particle interaction pairs i and j are governed by the Lennard-Jones (LJ) 12-6 potential:

$$U_{Lennard-Jones}(r_{ij}) = 4\varepsilon_{ij}\left[\left(\frac{\sigma_{ij}}{r_{ij}}\right)^{12} - \left(\frac{\sigma_{ij}}{r_{ij}}\right)^{6}\right] \quad (1)$$

Where r_{ij} denotes the distance between the particles, ε_{ij} denotes the potential well depth, and σ_{ij} is the closest distance of approach between i and j, also referred to as the effective size. ε values for each combination of main type and subtype are defined by the original MARTINI Force Field[28]. When used with special class particle types, ε_{ij} is scaled to 75% of its original value. σ is defined to be 0.47 nm for all normal particle types and 0.43 nm for special class particle types.

In addition to the LJ interactions, Q-type particles bearing a charge (q) interact via a Coulombic energy function:

$$U_{el}(r_{ij}) = \frac{q_i q_j}{4\pi\varepsilon_0\varepsilon_{rel}r_{ij}} \quad (2)$$

Where q_i and q_j are point charges, $1/4\pi\varepsilon0$ is Coulomb's constant, and r_{ij} denotes the distance between the particles. The dielectric constant ε_{rel} varies depending on the type of solvent (see Section 2.3 for further clarification).

To avoid unwanted noise, both of these potential energy functions are used in their shifted form, in which both the energy and force become zero at the cutoff distance r_{cut} = 1.2 nm. The LJ potential is shifted from r_{shift} = 0.9 nm to r_{cut} and the electrostatic potential is shifted from r_{shift} = 0.0 nm to r_{cut}. Shifting the potential energy functions as such allows for the imitation of distance-dependent screening. Nonbonded interactions between nearest neighbors are excluded from these calculations.

2.2.2 *Bonded Interactions*

Bonded interactions between chemically connected sites are modeled by a set of four harmonic potential energy functions acting between the bonded sites i, j, k, and l. The first equation characterizes chemical bonds through the bond potential V_{bond}:

$$V_{bond}\left(d_{ij}\right) = \frac{1}{2} K_{bond}\left(d_{ij} - d_{bond}\right)^2 \tag{3}$$

Where K_{bond} is the force constant and d_{bond} is the equilibrium bond distance. LJ interactions are ignored between bonded particles.

The second equation represents chain stiffness through the angle potential V_{angle}:

$$V_{angle}\left(\varphi_{ijk}\right) = \frac{1}{2} K_{angle}\left[\cos\left(\varphi_{ijk}\right) - \cos\left(\varphi_{angle}\right)\right]^2 \tag{4}$$

Where K_{angle} is the force constant and φ_{angle} is the equilibrium angle. LJ interactions between second nearest neighbors are included.

The third equation describes the improper dihedral angle potential V_{ID} which is used to prevent out-of-plane distortion of planar groups:

$$V_{ID}(\psi_{ID}) = K_{ID}\left(\psi_{ijkl} - \psi_{ID}\right)^2 \tag{5}$$

Where K_{ID} is the force constant and ψ_{ID} is the equilibrium angle.

The fourth equation models the proper dihedral angle V_D which imposes secondary structure on the peptide backbone:

$$V_D(\psi_{ijkl}) = K_D[1 + \cos(n\psi_{ijkl} - \psi_D)] \tag{6}$$

Where K_D is the force constant, n is the periodicity (the number of allowable minima in the interval as the molecule rotates), and ψ_D is the equilibrium improper dihedral angle.

The parameters of these four equations vary depending on the location of the bead in the peptide and the type of peptide. Peptide backbone beads are dependent on the secondary structure of the peptides but not the specific amino acids. Backbone-side chain and side chain-side chain parameters are conversely dependent on the specific amino acids and not secondary structure. Backbone-backbone-side chain and backbone-side chain-side chain bond angles and force constants are independent of both secondary structure and amino acid. Table 2.1[32] contains the backbone bonded parameters. The force constants presented are to be used when the backbone beads all have the same secondary structure;

Table 2.1. Backbone bonded parameters for each of the different secondary structures supported by the MARTINI force field. (Reprinted with permission from L. Monticelli, S. K. Kandasamy, X. Periole, R. G. Larson, D. P. Tieleman and S.-J. Marrink, *Journal of Chemical Theory and Computation*, 2008, **4**, 819–834. Copyright © 2007, American Chemical Society.)

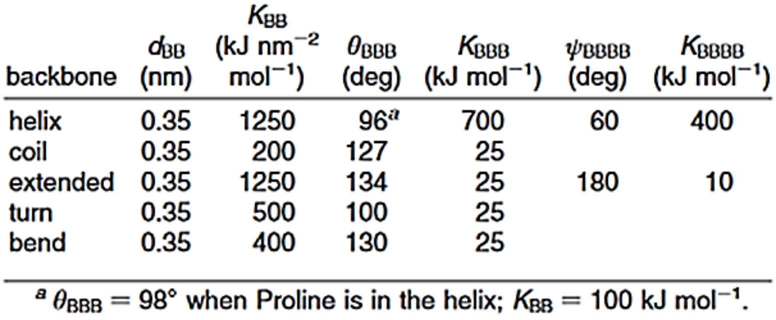

backbone	d_{BB} (nm)	K_{BB} (kJ nm^{-2} mol^{-1})	θ_{BBB} (deg)	K_{BBB} (kJ mol^{-1})	ψ_{BBBB} (deg)	K_{BBBB} (kJ mol^{-1})
helix	0.35	1250	96^a	700	60	400
coil	0.35	200	127	25		
extended	0.35	1250	134	25	180	10
turn	0.35	500	100	25		
bend	0.35	400	130	25		

[a] $\theta_{BBB} = 98°$ when Proline is in the helix; $K_{BB} = 100$ kJ mol^{-1}.

if the backbone beads contain multiple secondary structures, the weaker force constant is used.

Table 2.2. Equilibrium angles, improper dihedral angles, and the corresponding force constants for each categorized by amino acid. The amino acids who force constants are not specified are categorized as constraints in the topology file. (Reprinted with permission from L. Monticelli, S. K. Kandasamy, X. Periole, R. G. Larson, D. P. Tieleman and S.-J. Marrink, *Journal of Chemical Theory and Computation*, 2008, **4**, 819–834. Copyright © 2007, American Chemical Society.)

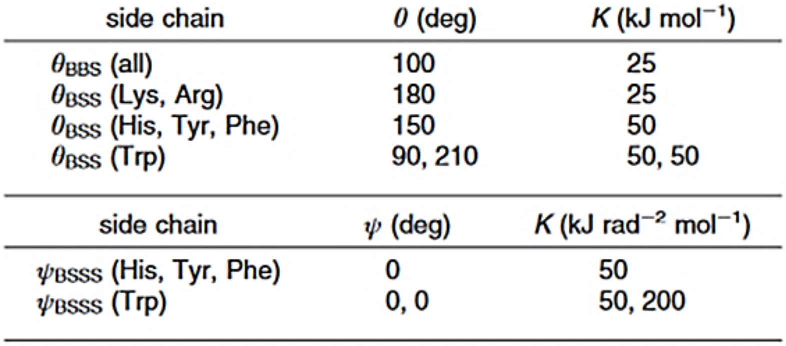

side chain	θ (deg)	K (kJ mol^{-1})
θ_{BBS} (all)	100	25
θ_{BSS} (Lys, Arg)	180	25
θ_{BSS} (His, Tyr, Phe)	150	50
θ_{BSS} (Trp)	90, 210	50, 50

side chain	ψ (deg)	K (kJ rad^{-2} mol^{-1})
ψ_{BSSS} (His, Tyr, Phe)	0	50
ψ_{BSSS} (Trp)	0, 0	50, 200

Table 2.2[32] shows the bond angles of peptides with side chains, and Table 2.3[32] shows the bonds lengths and force constants for amino acids with side chains.

Table 2.3. Bond lengths and corresponding force constants for amino acids with side chains. The amino acids who force constants are not specified are categorized as constraints in the topology file. (Reprinted with permission from L. Monticelli, S. K. Kandasamy, X. Periole, R. G. Larson, D. P. Tieleman and S.-J. Marrink, *Journal of Chemical Theory and Computation*, 2008, **4**, 819–834. Copyright © 2007, American Chemical Society.)

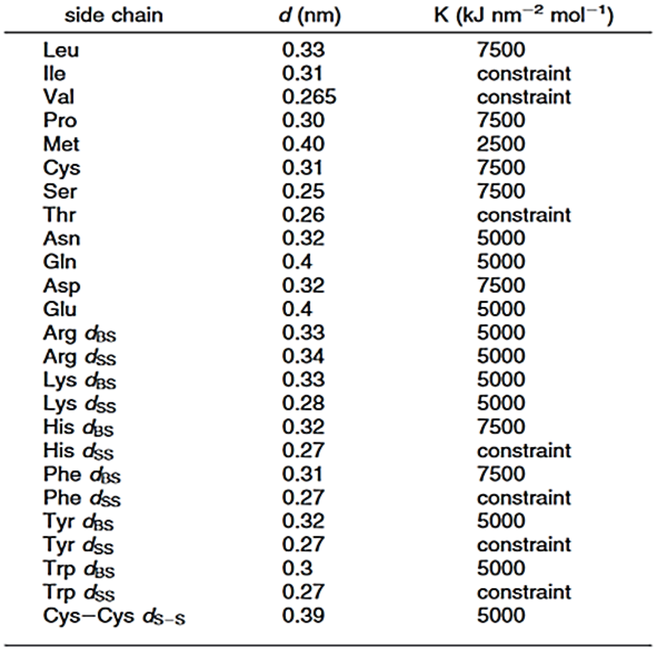

side chain	d (nm)	K (kJ nm^{-2} mol^{-1})
Leu	0.33	7500
Ile	0.31	constraint
Val	0.265	constraint
Pro	0.30	7500
Met	0.40	2500
Cys	0.31	7500
Ser	0.25	7500
Thr	0.26	constraint
Asn	0.32	5000
Gln	0.4	5000
Asp	0.32	7500
Glu	0.4	5000
Arg d_{BS}	0.33	5000
Arg d_{SS}	0.34	5000
Lys d_{BS}	0.33	5000
Lys d_{SS}	0.28	5000
His d_{BS}	0.32	7500
His d_{SS}	0.27	constraint
Phe d_{BS}	0.31	7500
Phe d_{SS}	0.27	constraint
Tyr d_{BS}	0.32	5000
Tyr d_{SS}	0.27	constraint
Trp d_{BS}	0.3	5000
Trp d_{SS}	0.27	constraint
Cys–Cys d_{S-S}	0.39	5000

2.3 Coarse-Grained Parameterization Based on Particle Types

There are three particle types of interest for the computational studies presented in this work: amino acid particles, water particles, and ion particles.

2.3.1 Amino Acid Mapping

The characterization of the twenty natural amino acids by their main interaction site can be seen in Figure 2.1[32]. The characterization of the backbone beads is dependent on the secondary structure of the protein: dispersed in solution or in a coil or bend [P] or part of a helix or β-sheet [N]. All this information combined results in the parameterization shown in Table 2.4[32].

Table 2.4. Backbone particle types based upon different kinds of secondary structure. What the characterization implies about the particle is specified in Section 2.1. (Reprinted with permission from L. Monticelli, S. K. Kandasamy, X. Periole, R. G. Larson, D. P. Tieleman and S.-J. Marrink, *Journal of Chemical Theory and Computation*, 2008, **4**, 819–834. Copyright © 2007, American Chemical Society.)

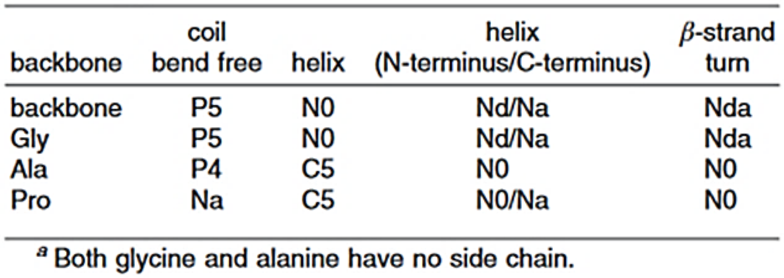

backbone	coil bend free	helix	helix (N-terminus/C-terminus)	β-strand turn
backbone	P5	N0	Nd/Na	Nda
Gly	P5	N0	Nd/Na	Nda
Ala	P4	C5	N0	N0
Pro	Na	C5	N0/Na	N0

[a] Both glycine and alanine have no side chain.

Peptide side chain characterization is based upon the main type of the side chain: apolar amino acids (Leu, Pro, Ile, Val, Cys, and Met) are C-type, polar, uncharged amino acids; (Thr, Ser, Asn, and Gln) are P-type, amino acids with small, negative side chains; (Glu and Asp) are Q-type, amino acids with positive side chains; (Arg and Lys) are Q-type with the inclusion of uncharged particle; ring-based amino acids (His, Phe, Tyr, and Trp) are special class. The values of these parameters are experimentally validated through a comparison of the free energy of partitioning between oil and aqueous phases. The main and subtype of each amino acid side chain as well as the experimental validation data can be found in Table 2.5[32]. Note that in an update to the model[33], the parameters of some of the peptides are updated to better confer with the parameterization of AA force fields.

Table 2.5. Side chain particle types based upon different kinds of secondary structure. What the characterization implies about the particle is specified in Section 2.1. (Reprinted with permission from L. Monticelli, S. K. Kandasamy, X. Periole, R. G. Larson, D. P. Tieleman and S.-J. Marrink, *Journal of Chemical Theory and Computation*, 2008, **4**, 819–834. Copyright © 2007, American Chemical Society.)

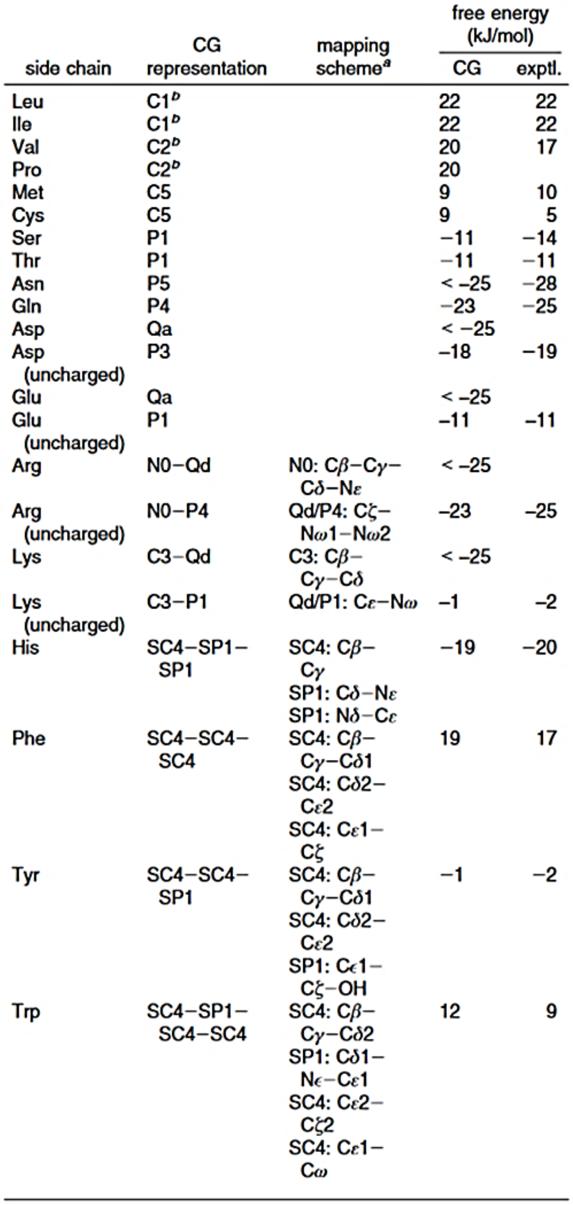

side chain	CG representation	mapping scheme[a]	free energy (kJ/mol)	
			CG	exptl.
Leu	C1[b]		22	22
Ile	C1[b]		22	22
Val	C2[b]		20	17
Pro	C2[b]		20	
Met	C5		9	10
Cys	C5		9	5
Ser	P1		−11	−14
Thr	P1		−11	−11
Asn	P5		< −25	−28
Gln	P4		−23	−25
Asp	Qa		< −25	
Asp (uncharged)	P3		–18	–19
Glu	Qa		< –25	
Glu (uncharged)	P1		–11	–11
Arg	N0−Qd	N0: Cβ−Cγ−Cδ−Nε	< –25	
Arg (uncharged)	N0−P4	Qd/P4: Cζ−Nω1−Nω2	–23	–25
Lys	C3−Qd	C3: Cβ−Cγ−Cδ	< –25	
Lys (uncharged)	C3−P1	Qd/P1: Cε−Nω	–1	–2
His	SC4−SP1−SP1	SC4: Cβ−Cγ SP1: Cδ−Nε SP1: Nδ−Cε	−19	−20
Phe	SC4−SC4−SC4	SC4: Cβ−Cγ−Cδ1 SC4: Cδ2−Cε2 SC4: Cε1−Cζ	19	17
Tyr	SC4−SC4−SP1	SC4: Cβ−Cγ−Cδ1 SC4: Cδ2−Cε2 SP1: Cϵ1−Cζ−OH	−1	−2
Trp	SC4−SP1−SC4−SC4	SC4: Cβ−Cγ−Cδ2 SP1: Cδ1−Nϵ−Cε1 SC4: Cε2−Cζ2 SC4: Cε1−Cω	12	9

2.3.2 Water Mapping

There are currently two main water models available for use with the MARTINI Force Field: standard water beads[28] and polarized water beads[34]. Four standard water molecules are modeled as one P_4 water bead. These standard water beads lack charge and therefore ignore the effects of electrostatic fields and molecular polarization[34]. The simple one bead model allows for the insertion of large amounts of water with minimal extra computational burden added to a simulation. However, standard water beads also have a higher freezing point than that of normal water; freezing of standard water beads occurs via nucleation and cannot be counteracted once started. A simple solution to this is the inclusion of additional stochastic forces of an antifreeze agent into the system. MARTINI created their own antifreeze particle called Big P_4 (BP_4), which disrupts the uniform lattice packing of the normal P_4 water beads and helps prevent the development of nucleation sites in a simulation. The ratio of standard water beads to antifreeze beads to prevent the development of nucleation sites at or above the freezing point of water is 9:1. This ratio affects solvent properties slightly, but has been shown to have no significant change on simulations overall.

Polarized water beads were introduced to the MARTINI Force Field as a way to compensate for the lack of explicit polarization in standard water, as implicitly applying electrostatic interactions can produce problems in systems with charged particles and those with multiple phases. Polarized water beads consist of three separate particles inside one bead, compared to standard water which has one particle, as seen in Figure 2.2. The central particle, W, is neutral and interacts with other particles via LJ interaction level III[28]. The WP and WM particles are attached to W via a constraint with a distance 0.14 nm and carry a positive and negative charge of +q and -q, respectively, where $q = 0.46$. The constraint distance prevents the overlap of charged particles in adjacent water beads and accurately represent the instantaneous dipole of the four water molecules the polarized bead represents. The chosen charge produces dielectric constants which are the closest to experimental values at room temperature[35]. A harmonic angle potential with an equilibrium angle $\theta = 0$ allows for a vanishing dipole moment and a force constant $K_\theta = 4.2$ kJ mol^{-1} rad^{-2} also provides a close approximation of experimental values of the dielectric constant of water. WP and WM lack any LJ interactions, interacting via a Coulomb function only, and do not interact with each other inside the same water bead, allowing the rotation of the two charged particles around W. Due to the inclusion of the additional particles inside of the water bead, polarized water beads have a stronger attraction to one other than standard water beads. Therefore, when using polarizable water, to ensure realistic behavior the global dielectric constant must be reduced from the $\varepsilon_r = 15$ used with standard water to $\varepsilon_r = 2.5$.

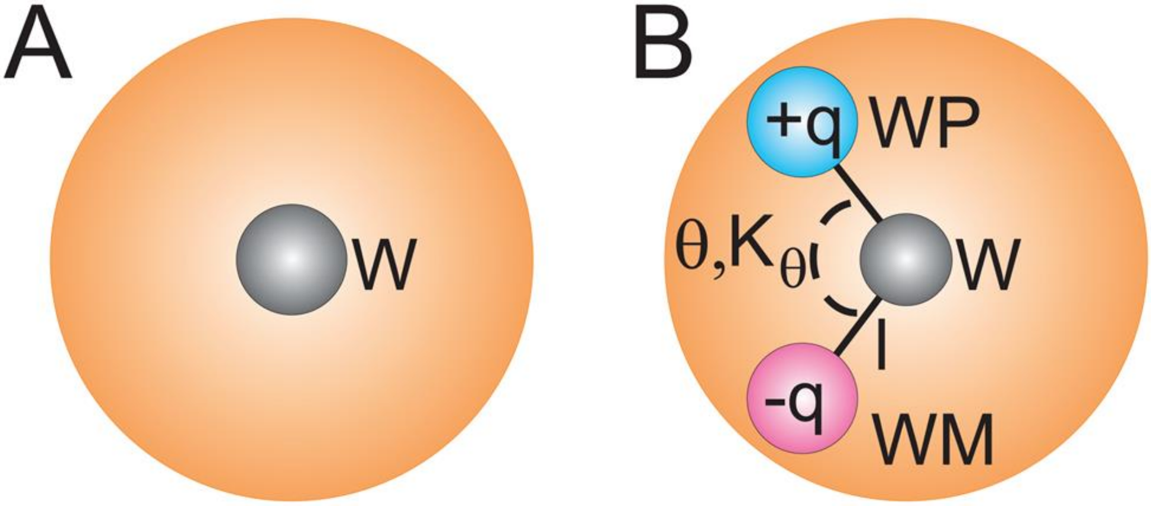

Figure 2.2. A comparison of MARTINI standard water (A) and MARTINI polarizable water (B). The orange sphere is the van der Waals radii of particle W. (Yesylevskyy SO, Schäfer LV, Sengupta D, Marrink SJ (2010) Polarizable Water Model for the Coarse-Grained MARTINI Force Field. PLoS Comput Biol 6(6): e1000810. https://doi.org/10.1371/journal.pcbi.1000810. Copyright: © 2010 Yesylevskyy et al.)

2.3.3 Ion Mapping

MARTINI CG ions are represented as Q-type particles.

2.4 Time Scale Interpretation

The larger particle sizes used in MARTINI CG modeling present a smoother energy landscape than those of atomistic models. The reduction in friction arising from fewer degrees of freedom creates an increase in the diffusion dynamics of MARTINI CG simulations by a factor of four[28]. Therefore, two types of time can be discussed in regard to MARTINI simulations: a simulation time and an effective time, the latter of which is the simulation time with the scaling factor of four applied. Throughout this manuscript, unless otherwise stated, effective time is assumed.

Chapter 3

Hybrid Aromatic Ultra-Short Peptide System

3.1 Overview of Diphenylalanine and Molecular Composition

Diphenylalanine (FF) is a stable, ultra-short peptide which has been extensively researched using experimental[36-44] and computational[44-46] approaches. In more recent years, derivatives of FF such as triphenylalanine (FFF) and diphenylalanine-fluorenylmethyloxycarbonyl chloride (FF-Fmoc) have been investigated to determine if these peptide compounds are capable of self-assembling into identifiable nanostructures[47]. FF has been reported to form distinct nanostructures such as vesicles and nanotubes[45,46,48], while its derivatives have assembled into nanowires, nanofibers, and ribbons[47]. The primary focus of the above studies has been the development of nanostructures from a single peptide sequence; however, the creation of biological materials with specific properties can also be achieved through the inclusion of multiple peptide sequences. A variation in sequence allows for the generation of sequence-specific properties, which can create materials with controllable, unique properties and characteristics.

A 2014 computational study by Guo et al.[47], whose results were experimentally verified, reports that in mixtures of FF and FFF, the resulting nanostructures formed were toroidal in nature. The formation of nanostructures demonstrates the influence of sequence-specific properties, though there is a general lack of understanding on how altering peptide sequences can affect the properties of biological materials. Additionally, research into the mechanisms of self-assembly of distinct peptide sequences in the formation of a hybrid biological material with targeted properties is sparse.

In this study, the impact of molecular composition on the morphology of hybrid self-assembled biological peptide materials was examined using FF and its derivative phenylalanine-asparagine-phenylalanine (FNF), which was chosen for the extra polarity injected into FF by the addition of asparagine. The molecular composition was varied in two ways: by varying the total peptide concentration in the system and the relative tripeptide (FNF) concentration in the system from 0-100%. Using two different peptide sequences also allowed for the study of how variation in polar groups impacts morphological changes in self-assembled hybrid materials. A computational approach (CG MD simulations) was employed to address the large parameter space. The results from this study provide insight into the assembly mechanisms of specific peptide sequences and the influence of molecular composition on nanostructure formation, where it is shown that both the total peptide concentration and relative tripeptide concentration affect the morphology of hybrid biological assemblies.

3.2 Model Parameterization and Computational Methods

3.2.1 Topology Design

MD simulations were employed to study the dynamics of the peptide aggregation process along with the structure and morphology of the resulting hybrid biological materials. To capture the assembly process from dispersed peptides in solvent to a fully formed hybrid assembly, several thousands of molecules had to be simulated. Using an AA representation was not feasible as the temporal scales needed to observe the assembly process as well as capture the structural properties of the assembled hybrid materials would have resulted in simulations that were too resource-intensive. Therefore, the simulations were built using a CG representation, namely the MARTINI CG force field (v2.2). Coarse-grained representations of both FF and FNF are shown in Figure 3.1 with FF represented in (a) and FNF represented in (b). Particle type P5 was used to represent the phenylalanine backbone (orange) while three SC5 beads were used for the aromatic side chain (blue). Particle type P5 was used for both the backbone and side chain bead of asparagine (green and purple, respectively). The peptides were assumed to be uncapped, with charges at both the N and C termini, allowing for the system to exist at a charge neutral state.

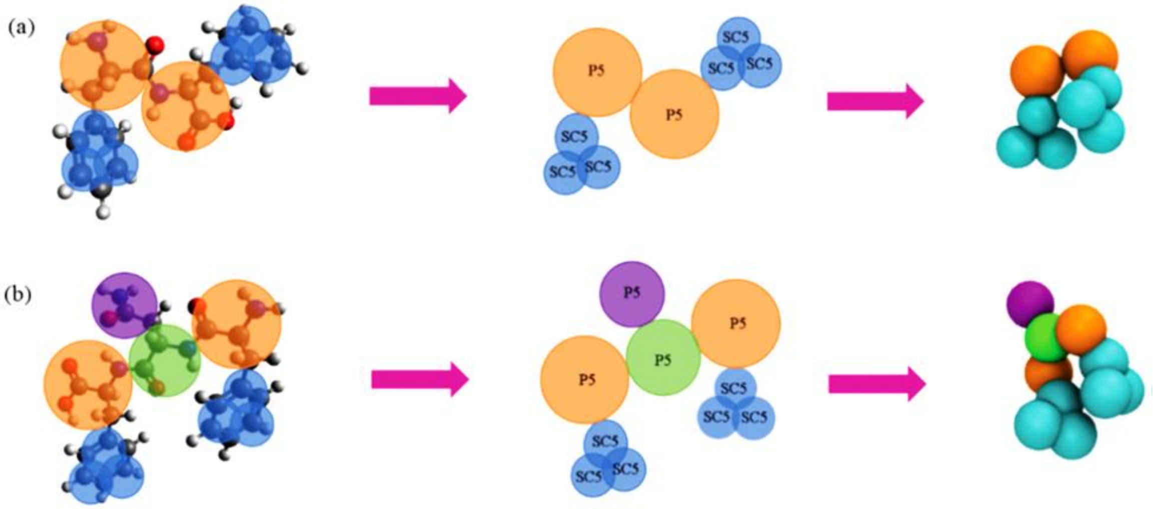

Figure 3.1. Coarse-grained representations of (a) diphenylalanine (FF) and (b) phenylalanine-asparagine-phenylalanine (FNF). The left-most picture shows the MARTINI approximation over an AA model of the peptides. The middle picture details the MARTINI particle types assigned to each approximation, and the last picture shows the MARTINI representation of the peptide.

3.2.2 Simulation Parameters

Simulations were built using the GROMACS software package (v5.2.1)[50-53]. Using commands innate to the package, the FF and FNF peptides were inserted into a simulation box and solvated with standard water and the standard ratio of anti-freeze particles[28]. To remove any overlaps due to the random particle insertion, the system was energy minimized using a steepest descent integrator. Once overlaps were accounted for, the system parameters were brought to experimental values through a 500 ps equilibration. Once the system was ready for production, each simulation was run for 4 μs, which was chosen to ensure the formation of a single, stable, self-assembled nanostructure.

All of the simulations were run in the isothermal-isobaric ensemble. The total number of peptides in each simulation was 500. The temperature was maintained at 310 K[45,47] using velocity rescaling with a stochastic term to ensure correct sampling[54,55]. The pressure was maintained at 1 bar using the Parrinello-Rahman barostat[56,57]. The timestep for each simulation was 25 fs. The neighbor lists were updated every 0.25 ps with a cut-off of 1.2 nm, and the particle trajectories were sampled every 0.25 ps. The LINCS algorithm[58] was used to constrain the bonds of the aromatic phenylalanine side chains.

Overall, five total peptide concentrations (0.1, 0.15, 0.2, 0.25, and 0.3 peptides/nm^3) and eleven relative tripeptide concentrations (from 0% to 100%) were simulated. The total peptide concentration was varied by pre-selecting a starting box size and populating it with the appropriate number of solvent beads. The relative tripeptide concentration was varied by adjusting the ratio of FF to FNF beads in a system while keeping the total peptide count at 500. Each of these 55 resulting simulations were run on ten independent particle trajectories for statistical significance, for a total of 550 simulations on which the result and analyses are based.

3.3 Simulation Results of 55 Unique Molecular Compositions

All molecular compositions were observed to spontaneously self-assemble into identifiable nanostructures, each composed of an FF-FNF bilayer formed via the hydrophobic effect. The hydrophobic effect occurs in this system as the hydrophobic, aromatic rings which make up the phenylalanine side chains preferentially interact with one another, minimizing their exposure to the solvent particles. The hydrophilic backbones of phenylalanine and asparagine as well as asparagine's side chain, in contrast, preferentially interact with the solvent particles. These processes occur simultaneously, and drive peptide aggregation until the system is at its lowest energy configuration, represented by the single, stable aggregate formed[55,57,59-62].

3.3.1 Morphological Variation Quantified

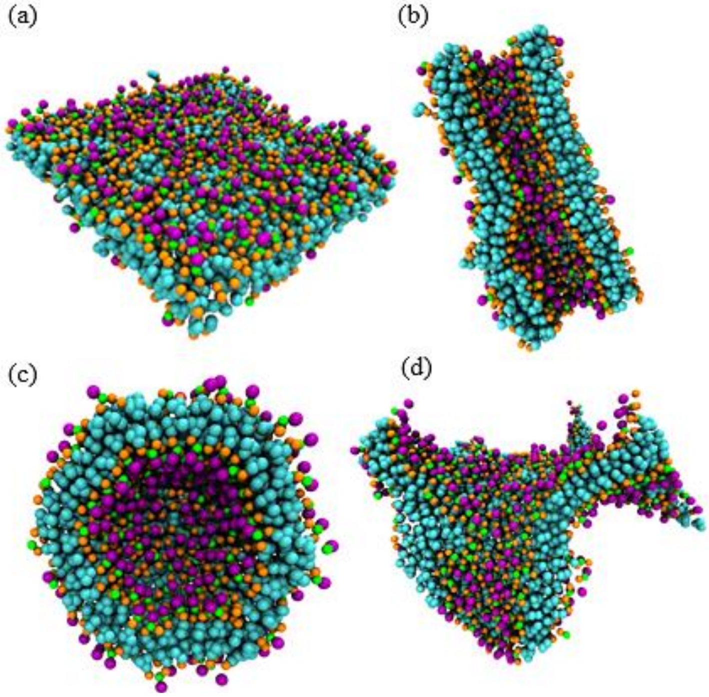

Figure 3.2 Representative pictures of each of the four hybrid nanostructures formed in the phase space: (a) lamellar bilayer, (b) axial cross-sectional view of a nanotube, (c) diametrical cross-sectional view of a vesicle, and (d) disordered assembly.

Four categories of nanostructures were identified, with a representative of each morphology shown in Figure 3.2[49]. The nanostructures were classified based upon their morphology, with morphology defined by a nanostructure's relationship to the three spatial dimensions. A nanostructure was considered to be "open" in a given spatial direction (i) if it interacted with itself through any periodic walls, meaning the nanostructure extended indefinitely, or (ii) if two edges of the bilayer perpendicular to a direction were exposed to the solvent particles. A nanostructure was considered to be "closed" in a direction if it didn't meet either of these criteria. Therefore, a bilayer open in two directions with its edges exposed to solvent was classified as a lamella

Table 3.1 Summary of the four morphologies formed across the five total peptide concentrations and eleven relative tripeptide concentrations.

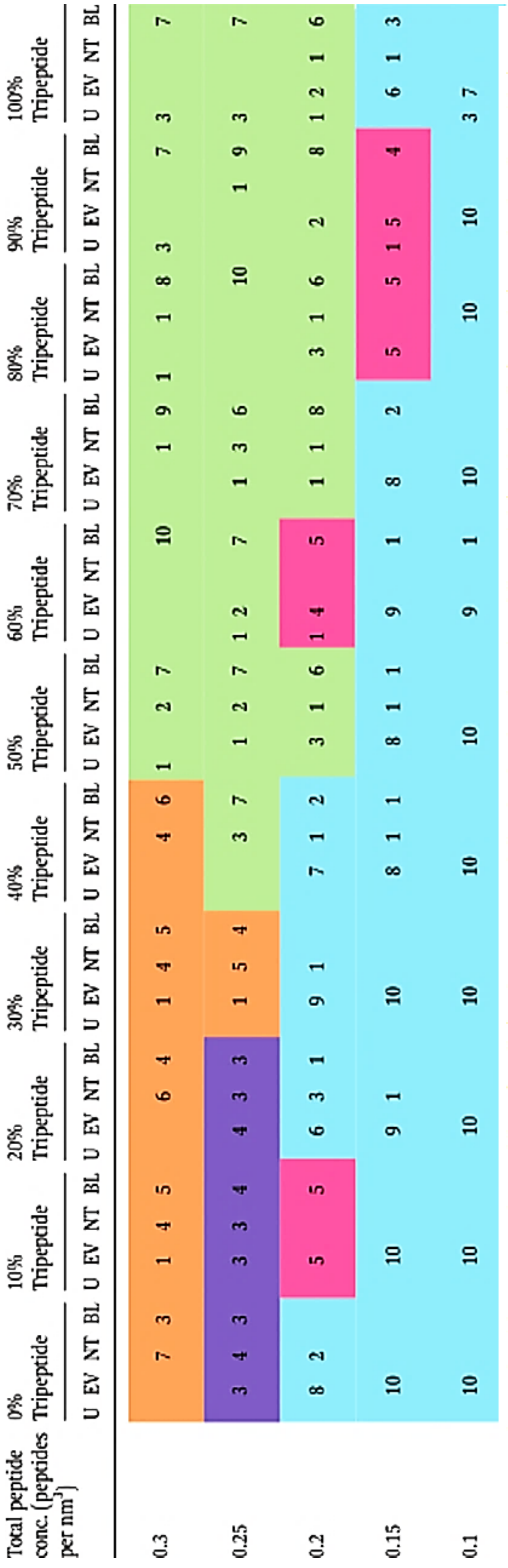

Total peptide conc. (peptides per nm^3)	0% Tripeptide				10% Tripeptide				20% Tripeptide				30% Tripeptide				40% Tripeptide				50% Tripeptide				60% Tripeptide				70% Tripeptide				80% Tripeptide				90% Tripeptide				100% Tripeptide			
	U	EV	NT	BL	U	EV	NT	BL	U	EV	NT	BL	U	EV	NT	BL	U	EV	NT	BL	U	EV	NT	BL	U	EV	NT	BL	U	EV	NT	BL	U	EV	NT	BL	U	EV	NT	BL	U	EV	NT	BL
0.3			7	3		1	4	5			6	4		1	4	5			4	6	1		2	7				10			1	9	1		1	8	3			7	3			7
0.25		3	4	3		3	3	4		4	3	3		1	5	4			3	7		1	2	7	1	2		7		1	3	6				10			1	9	3			7
0.2		8	2			5		5		6	3	1		9	1			7	1	2		3	1	6	1	4		5		1	1	8		3	1	6		2		8	1	2	1	6
0.15		10				10				9	1			10				8	1	1		8	1	1		9		1		8		2		5		5	1	5		4		6	1	3
0.1		10				10				10				10				10				10				9		1		10					10			10			3	7		

EV: elongated vesicle, NT: nanotube, BL: bilayer (lamellar) and U: unstructured/disordered. Color scheme is as follows: pink (vesicles/lamellae), purple (nanotubes/lamellae/vesicles), orange (nanotubes/lamellae), green (lamellar bilayers), and cyan (vesicles)

(Figure 3.2a), a bilayer closed in two directions but extending indefinitely in the third direction was a nanotube (Figure 3.2b), and a bilayer closed in all three directions was a vesicle (Figure 3.2c). In Figure 3.2b and Figure 3.2c, a cross-sectional view is provided to show the presence of a stabilized, internal cavity which can interact with the solvent. The fourth morphological category classified "disordered" nanostructures, in which the peptides locally organized themselves into a bilayer but did not fall into any of the three previous categories of lamella, nanotubes, or vesicles (Figure 3.2d).

A summary of morphological variation due to different molecular compositions is found in Table 3.1**[49]**. To better visualize the effects of total peptide concentration and relative tripeptide concentration, the results in Table 1 are further broken down into four histograms, one for each type of defined morphological structure. Each histogram shows the frequency with which a specific nanostructure occurred for each molecular composition simulated. Figure 3.3**[49]** shows the statistical occurrences of vesicle formation, which were consistently observed at lower total peptide concentrations (0.1 - 0.15 peptides/nm^3).

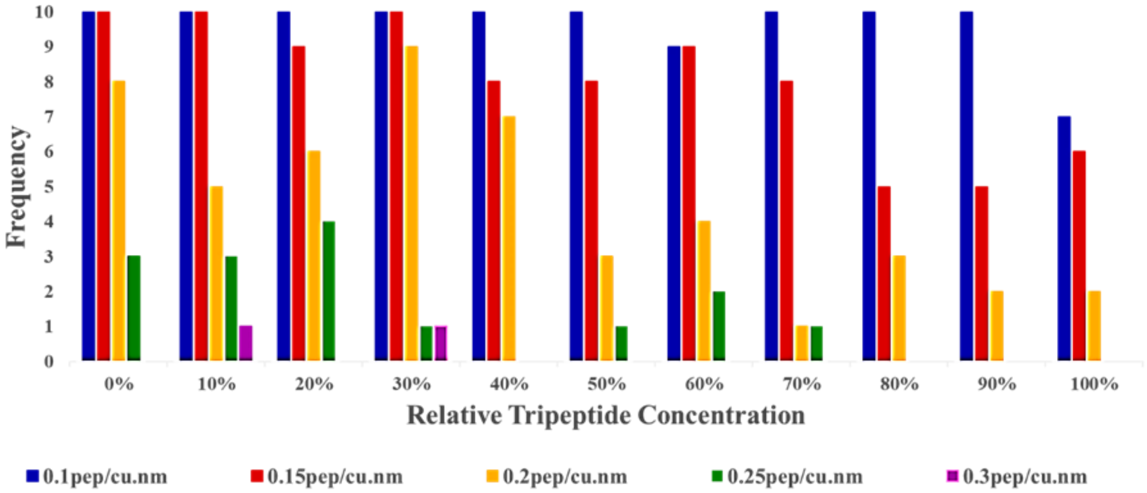

Figure 3.3. Histogram of the occurrence of vesicles in the phase space for different molecular compositions. These measurements used 10 independent particle trajectories for each molecular composition.

As the total peptide concentration increased, the tendency of the systems to form vesicles also decreased, a trend across all eleven relative tripeptide concentrations. At higher values of total peptide concentration (0.25-0.3 peptides/nm^3), lamellar bilayers began to occur with higher frequency, as seen in Figure 3.4[49]. They were also observed at a total peptide concentration of 0.2 peptides/nm^3, however only at high relative tripeptide concentrations (70%-100%).

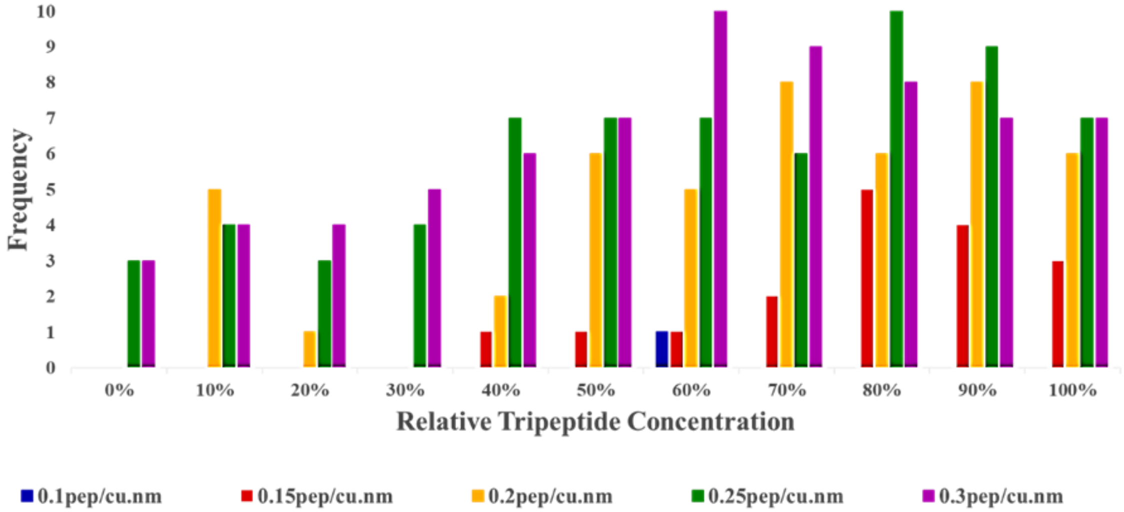

Figure 3.4. Histogram of the occurrence of lamellar bilayers in the phase space for different molecular compositions. These measurements used 10 independent particle trajectories for each molecular composition.

Nanotubes were found infrequently at higher total peptide concentrations (0.2-0.3 peptides/nm^3) and at low and medium relative tripeptide concentrations (0%-50%). As shown in Figure 3.5[49], nanotubes were also seen when the relative tripeptide concentration was high, though statistically these occurrences were rare.

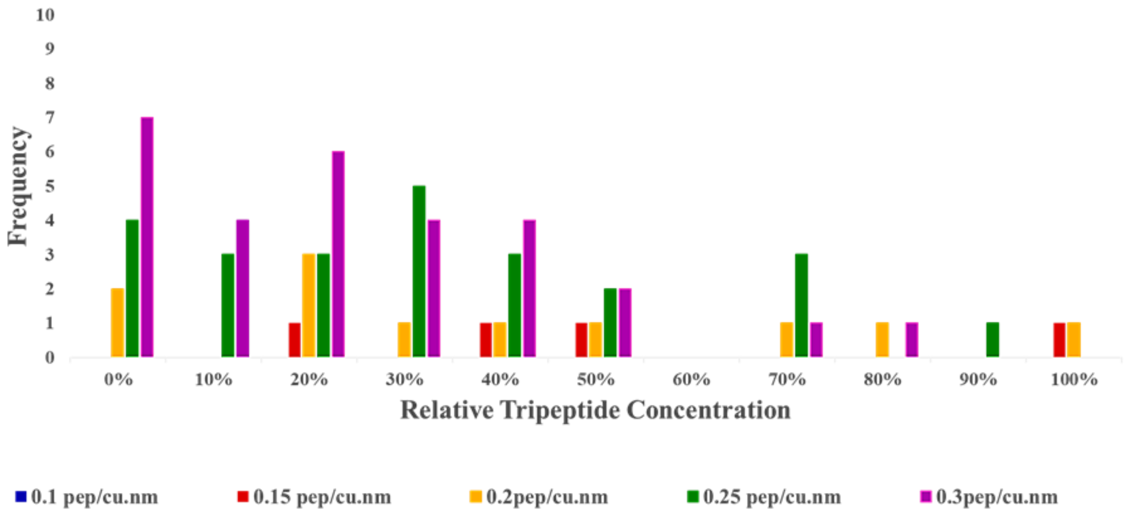

Figure 3.5. Histogram of the occurrence of nanotubes in the phase space for different molecular compositions. These measurements used 10 independent particle trajectories for each molecular composition.

Figure 3.6[49] shows that the rarest occurrence was that of a disordered assembly, which only occurred at higher relative tripeptide concentrations (90%-100%).

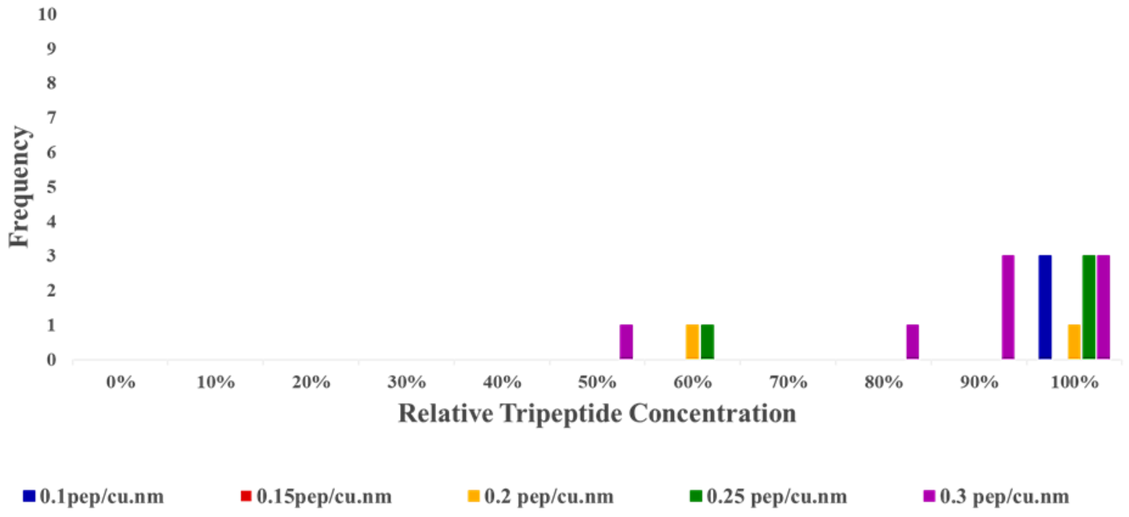

Figure 3.6. Histogram of the occurrence of disordered nanostructures in the phase space for different molecular compositions. These measurements used 10 independent particle trajectories for each molecular composition.

3.3.2 Assembly Pathways

The data composing the histograms indicated that the nanostructure assembly pathways were dependent on the relative tripeptide concentration of a system. Pure FF has been shown experimentally and with Monte Carlo simulations to form nanostructures in a concentration-dependent manner, starting at vesicles and progressing to nanotubes and then lamellae[63]. The same transitions were observed here at similar dipeptide concentrations, supporting the assumption that the nanostructures were at equilibrium. In addition, Guo et al.[45] reported that, in pure FF systems, smaller vesicles fused into larger ones at low total peptide concentrations. As the total peptide concentration increased, bilayers would instead fold into nanotubes. These phenomena are observed in Figure 3.7[49]; at low total peptide concentrations (0.1-0.15 peptides/nm^3), small vesicles assemble in the solvent until they encounter other small vesicles and coalesce to form larger-sized vesicles (Figure 3.7a). At higher values of relative tripeptide concentration, the peptides assemble into a bilayer which either stabilizes itself through periodic boundary interactions or bends and closes its free edges to form a nanotube or a vesicle (Figure 3.7b).

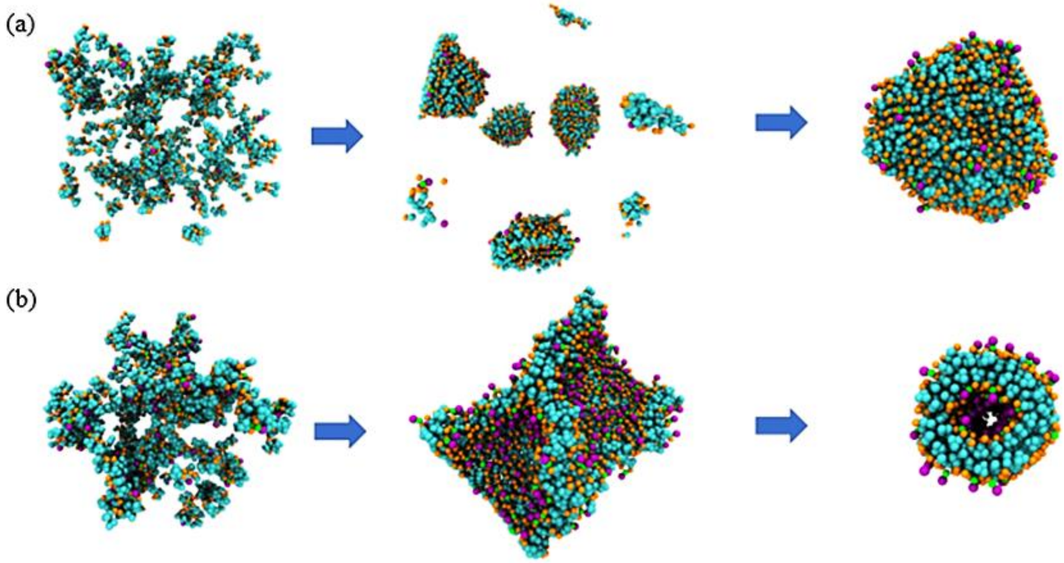

Figure 3.7. The assembly pathways reported in other works that are represented in this study's computational work. (a) At low total peptide concentrations, smaller vesicles fused to make larger ones. (b) At higher relative tripeptide concentrations, the peptides assembled into a bilayer which then folded into a nanotube.

The morphologies also depended on the relative concentrations of di- and tripeptides. As seen in Table 3.1, for all peptide ratios there was a preference for vesicle formation at the lowest total peptide concentrations and for lamellar bilayer formation at the highest total peptide concentrations. The relative tripeptide concentration acted as another degree of freedom which influenced nanostructure morphologies. From the statistics shown in Figures 3.3-3.6, a phase-space diagram (Figure 3.8**[49]**) was created to highlight the distinct influences both components of the molecular composition had on the formation of vesicles, nanotubes, and lamellar bilayers. At the bottom of the phase space, which is representative of low total peptide concentrations, the systems tended to be in the vesicle regime, as low total peptide concentrations are unable to form structures large enough to interact through periodic boundaries. In order to minimize the hydrophobic interactions of the aromatic phenylalanine rings, a fully-formed vesicle was the most favorable morphology.

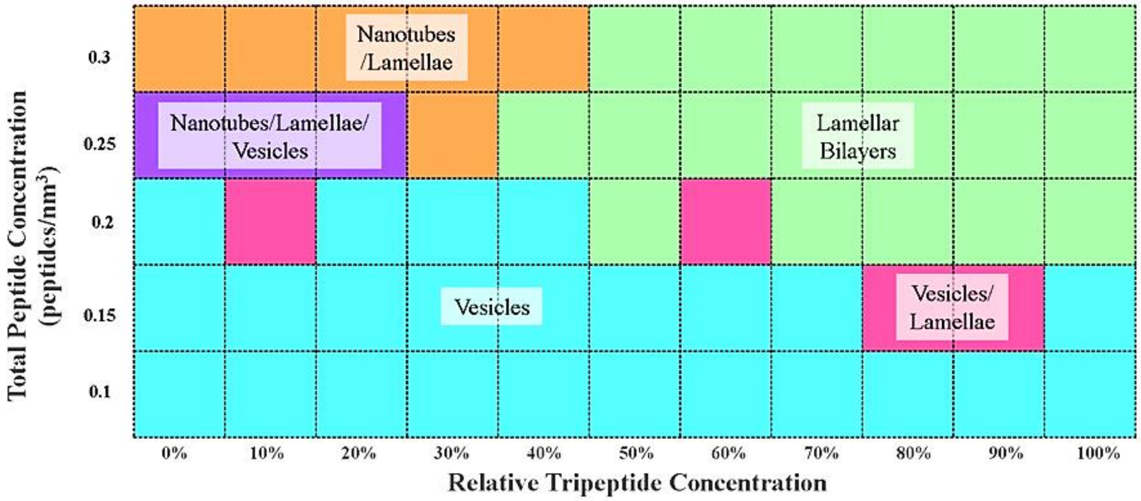

Figure 3.8. Phase space map of the four morphologies found at each total peptide concentration and each relative tripeptide concentration. The most representative structure of the ten simulations for that molecular composition is presented; if more than one structure was equally represented, all of those morphologies are presented.

At higher total peptide concentrations, the size of the aggregates increased, and the nanostructures formed in the systems had a higher tendency to interact through periodic boundaries and stabilize themselves. Nanostructures that interact with themselves can be categorized by the number of periodic boundaries they interact through: vesicles interact through none, nanotubes through two opposing, and lamella bilayers through four. This trend is displayed in Figure 3.8, where vesicles occurred at the lowest total peptide concentrations and nanotubes and lamellar bilayers began to replace vesicles at higher total peptide concentrations. In the upper left corner of Figure 3.8, there is an overlapping of the nanotube and lamellar bilayer regimes. This was attributed to two competing effects in the system: the propensity of the peptides to form lamellar bilayers at high total peptide concentrations, and the curvature added to the assembly due to the increase in the relative tripeptide concentration.

3.3.3 Influence of the Tripeptide on Nanostructure Formation

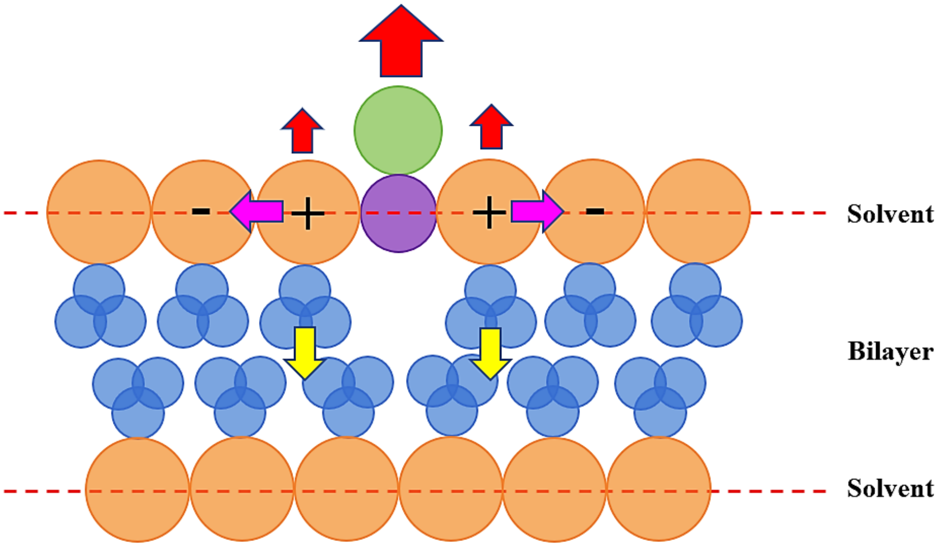

Figure 3.9. The pinching effect caused by the inclusion of FNF in a FF bilayer. The yellow arrows represent the hydrophobic attraction between the phenylalanine side chains, the red arrows represent the hydrophilic interactions between the peptide backbones, the asparagine side chains, and the solvent particles, and the purple arrows indicate electrostatic attractions.

The competing effects caused by the inclusion of the FNF tripeptide in a bilayer are specified in Figure 3.9[49]. The electrostatic attraction between the N and C termini of adjacent peptides and the favorable hydrophobic and hydrophilic interactions previously mentioned created a force differential within the bilayer. This, coupled with the hinge-like structure of the tripeptide due to the presence of asparagine as the middle residue, created a pinching effect on the bilayer and induced curvature.

To quantify the impact of the tripeptide hinge, the average angle between the backbone beads was measured. That data is shown in Figure 3.10[49]. The equilibrium angle in a single tripeptide is 107°; while in an FF/FNF bilayer, the angle of the tripeptide is approximately 113°. This indicates that the tripeptide is stretched along its backbone while the asparagine side chain in the middle of the tripeptide experiences an attractive force toward the solvent. This interaction keeps the hinge correctly aligned, and therefore causes local curvature to the bilayer.

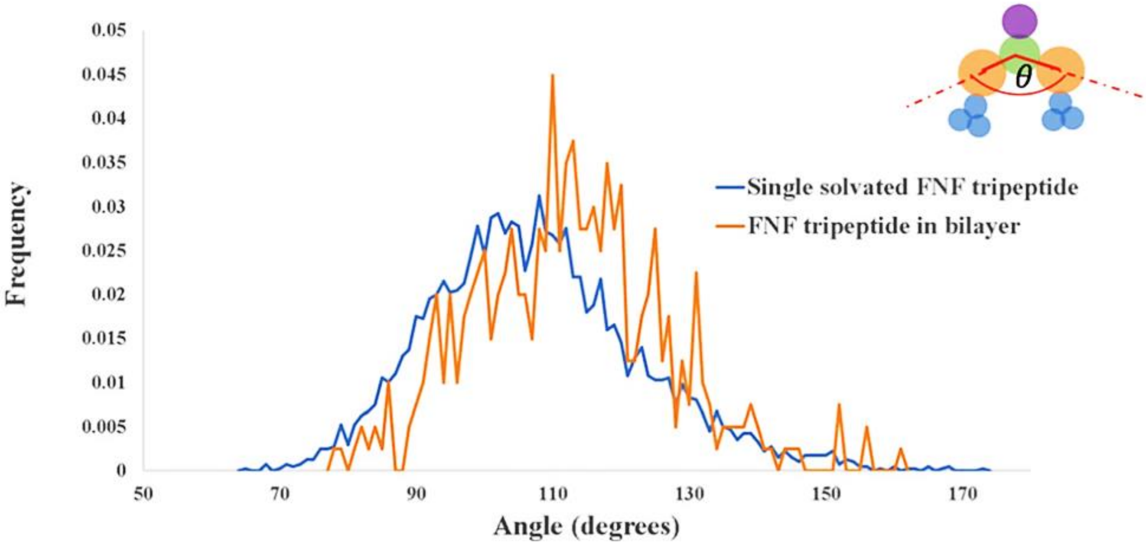

Figure 3.10. Distribution of the angle of the FNF backbone beads. The average angle is 112.9°, which is higher than the equilibrium angle of FNF at 107.4°.

In the upper right corner of Figure 3.8, the lamellar bilayer regime dominates. This due to the probability that the higher the relative tripeptide concentration, the higher the probability that FNF peptides will be distributed equally on both sides of the lamellar bilayer, therefore counteracting any local curvature that would occur in a specific direction. The distribution of FNF on a representative lamella bilayer is plotted in Figure 3.11**[49]**, where the closeness of the two peaks indicates the even distribution of the tripeptide on either side of the lamellar bilayer.

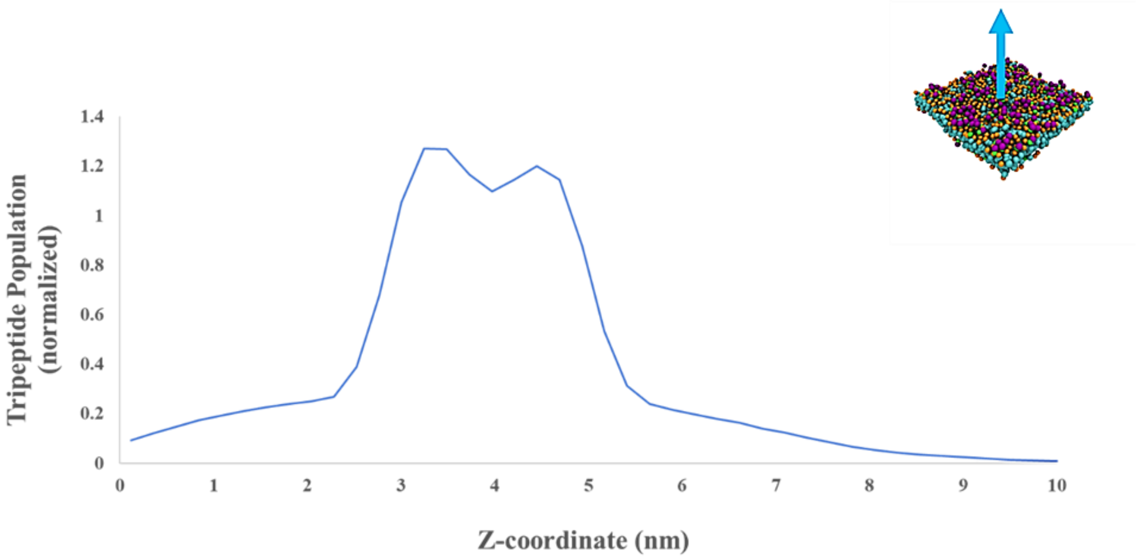

Figure 3.11. Density of FNF tripeptides plotted against the z-axis coordinate for the total peptide concentration 0.3 peptides/nm^3 and the relative tripeptide concentration 50%. Traveling through the lamellar bilayer results in two closely spaced peaks, indicating that the tripeptides are evenly distributed on the top and bottom of the lamellar bilayer.

A comparison between the distribution of the tripeptide in a lamellar bilayer between different morphologies is done in Table 3.2**[49]**. As expected, the larger number of tripeptides is found on the side of the bilayer that is external to the nanostructure as the tripeptides caused the bilayer to curve opposite the highest quantity of asparagine.

Table 3.2. Distribution of FNF on either side of a bilayer for the three different organized morphologies. The total peptide concentration is 0.25 peptides/nm^3 and the relative tripeptide concentration is 10%.

	Nanotube	Vesicle	Lamella
Inside	13	19	24 (top)
Outside	37	31	26 (bottom)

3.4 Conclusions of the Aromatic Peptide Study

The impact of molecular composition on the morphology of phenylalanine-based hybrid peptide materials was studied. CG MD simulations were used to study the morphology of peptide nanostructures composed of FF and FNF, two peptides with identical hydrophobic groups but different polar groups. The molecular composition of the systems was varied in two distinct ways, resulting in five total peptide concentrations and eleven relative tripeptide concentrations.

A rich polymorphism of hybrid peptide assemblies was presented. Distinct regimes in nanostructure were identified, and variation in the molecular compositions were shown to influence what morphologies occurred. Low tripeptide concentrations combined with high total peptide concentrations resulted in the greatest diversity in morphology, displaying vesicles, nanotubes, and lamellar bilayers. This diversity occurred due to the competing effects of a high total peptide concentration biasing the system toward lamellar bilayers and the presence of tripeptides inducing local curvature.

The results demonstrated the impact of molecular composition on phenylalanine-based hybrid biological materials and how the properties of those materials can be controlled. These findings can potentially inform the design of novel, hybrid peptide biological materials with desired morphologies and characteristics that can be easily targeted through the employment of distinct peptide sequences.

Chapter 4

Aliphatic Peptide Model Design

4.1 General Overview of A_6K and V_6K

The study of self-assembling amphiphilic peptides was popularized by Shuguang Zhang in the early 2000s[8,13,22,23,64-66]. Amphiphilic peptides, also described as surfactant-like peptides, mimic the lipid surfactant composition with a hydrophobic tail (composed of a chain of nonpolar amino acids) and a hydrophilic head (composed of at least one charged peptide residue)[65]. Conventionally, amphiphilic peptides contain a small number of residues, usually limited in size to between four and twelve residues. Self-assembling amphiphilic peptides have been found to have numerous substantiated uses throughout the medical field as their biocompatible, independent nature makes them ideal candidates for drug development[7-10], three-dimensional cell culturing[13-18], regenerative medicine[19-21], and many other biomedical applications. Two of the more well-studied peptide amphiphiles are A_6K (alanine-alanine-alanine-alanine-alanine-alanine-lysine) and V_6K (valine-valine-valine-valine-valine-valine-lysine). Both peptides have been shown experimentally to form stable nanostructures in solution[65,67]. The assembly mechanisms of the systems have been hypothesized to result from the hydrophobic effect as well as repulsion between the charged head groups[68].

In addition to experimental work, computational approaches have also been employed to study the nanostructures and assembly pathways of amphiphilic peptides A_6K and V_6K. Several AA studies[69-71] have been performed, which both validate experimental work and demonstrate the viability of a computational approach when researching amphiphilic peptides. A 2015 paper by Sun et al.[71] utilized MD simulations to investigate the secondary structures of A_6K and V_6K, with AA simulations determining peptide secondary structure and CG simulations determining self-assembly mechanisms and packing based upon peptide secondary structure. The paper by Sun et al. provides a comprehensive framework from which CG models of A_6K, V_6K, and their derivatives can be designed, validated, and used in further computational work.

In this study, topologies of A_6K and V_6K for use with the MARTNI CG framework were created. The development and validation of these two topologies resulted in the creation of three derivative models: A_6K_2, V_6K_2, and V_6K_3. The V_6K_2 topology was validated against experimental results successfully. A discussion of the studies utilizing the other two derivatives is located in Chapter 5.

4.2 Model Parameterization and Computational Methods

4.2.1 Topology Design

In order to develop feasible CG models of A_6K and V_6K, the secondary structure of the two peptides needed to be established. However, the reported secondary structures associated with each amphiphile were inconsistent as the experimental parameters in which the secondary structure is determined vary. It has been previously shown that environmental factors can influence secondary structure to the point that the propensity of a peptide to form a particular secondary structure can be overwritten[72]. Temporal factors can also affect which secondary structure is observed for a peptide, as the conformation of a peptide can change throughout the course of assembly[73]. A_6K is experimentally reported to show a variety of secondary structures: random coils[67,71,74-76], β-sheets[67,75-81], and α-helices[68,75] are the three most commonly reported secondary structures. This diversity in secondary structure can be attributed to the variation in environmental parameters in which these experiments are run. The proposed secondary structure of V_6K is much less varied, with a β-sheet conformation reported as the most common secondary structure[67,71].

A summary of the results from the 48 AA simulations performed by Sun et al. is shown in Figure 4.1[71]. Figure 4.1a depicts the propensity of the observed secondary structures in their simulations for the five middles residues of A_6K and V_6K in water. A_6K has an overwhelming propensity toward a coil conformation with some propensity toward a β-sheet conformation. V_6K is the exact opposite, having a high propensity toward a β-sheet conformation with some propensity toward a coil conformation. The results are further specified for all seven residues based upon the two highest conformations in Figures 4.1b and 4.1c. A_6K, along all seven residues, prefers to adopt a coil conformation though there is a slight propensity for the internal residues to adopt a β-sheet conformation. V_6K, on the internal five residues, prefers to adopt a β-sheet conformation; interestingly, the termini residues, like A_6K, overwhelmingly prefer a coil conformation. However, due to the limitations of the MARTINI framework in which the secondary structure is set throughout the entirety of the self-assembly process, a uniformity in secondary structure is easier to analyze. Therefore, in the topological development of A_6K, each of the seven MARTINI beads is assigned the coil secondary structure and each of the fifteen V_6K MARTINI beads is assigned the β-sheet (Extended) secondary structure.

The assignment of secondary structure determines the bond, constraint, angle, and dihedral parameters of the model. It also determines the bead type of each of the particles,

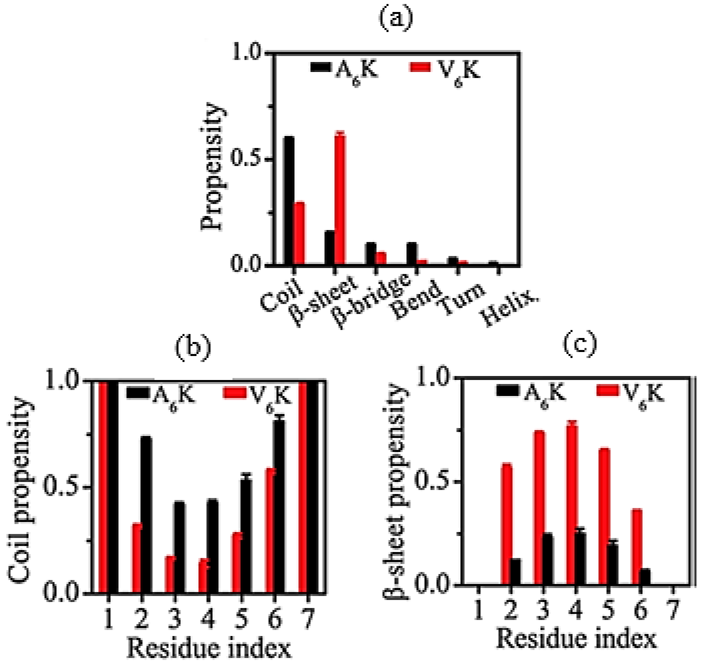

Figure 4.1. A summary of secondary structure propensity in A$_6$K and V$_6$K. (a) The average propensity of each detected secondary structure over the middle five residues of each peptide. (b) The propensity of the coil secondary structure in A$_6$K and V$_6$K. (c) The propensity of the β-sheet secondary structure in A$_6$K and V$_6$K. A$_6$K prefers to adapt a coil secondary structure, and V$_6$K prefers to adapt a β-sheet secondary structure. (Reprinted with permission from Y. Sun, Z. Qian, C. Guo and G. Wei, *Biomacromolecules*, 2015, **16**, 2940–2949. Copyright © 2015, American Chemical Society.)

which is specified for A$_6$K in Figure 4.2a and V$_6$K in Figure 4.2b. In A$_6$K, the alanine beads in the backbone (orange) were assigned the P4 particle types while the lysine bead in the backbone (pink) was assigned the P5 particle type. The side chain beads of lysine (blue), coming away from the backbone, were assigned the C3 and Qd particle types respectively. In V$_6$K, the valine backbone beads (green) as well as the lysine backbone bead (red) were assigned the Nda particle type. The valine side chain beads (yellow) were assigned the C2 particle type, and, like in A$_6$K, the lysine side chain beads (blue) were assigned the C3 and Qd particle types. The color of the lysine side chain beads was kept uniform for simplicity

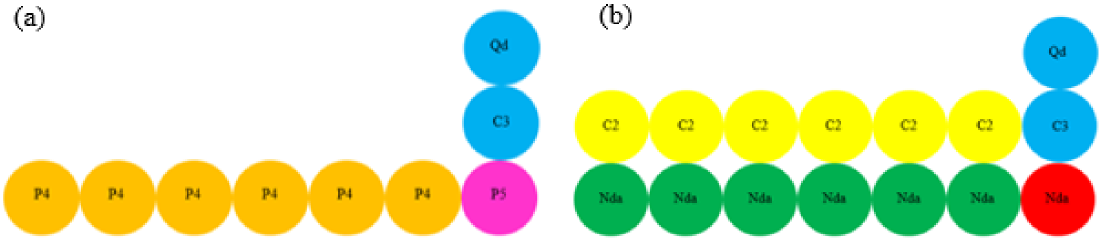

Figure 4.2. Coarse-grained representations of (a) A_6K (b) V_6K.

Figure 4.3 shows a comparison between an ideal AA model of A_6K and V_6K (a and b)**[67]**, an ideal CG model of A_6K and V_6K (c and d)**[71]**, and the actual peptides produced from the developed topologies when at a low energy minimum (e and f).

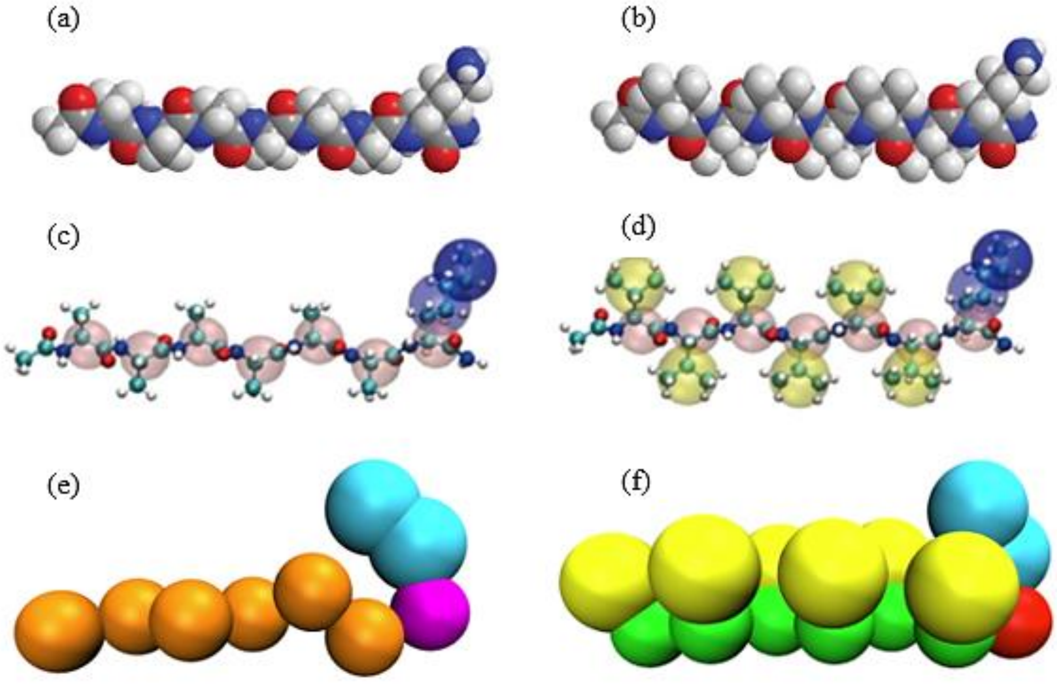

Figure 4.3. An AA representation, a CG ideal, and the MARTINI CG representations of the developed topologies for A_6K (a), (c), (e) and V_6K (b), (d), (f). (a) and (b): (Reproduced from Ref. 67 with permission from The Royal Society of Chemistry). (c) and (d): (Reprinted with permission from Y. Sun, Z. Qian, C. Guo and G. Wei, *Biomacromolecules*, 2015, **16**, 2940–2949. Copyright © 2015, American Chemical Society.)

Once the topologies for A_6K and V_6K were validated, topologies for derivatives of both peptides were developed, resulting in models for A_6K_2, V_6K_2, and V_6K_3. The inclusion of additional lysine residues did not warrant any changes (i.e., secondary structure) in the topology. Representative peptides of the modeled topologies at a low energy minimum are seen in Figure 4.4. Only results for V_6K_2 will be presented as components of that study have been completed in their entirety and therefore can be confidently reported.

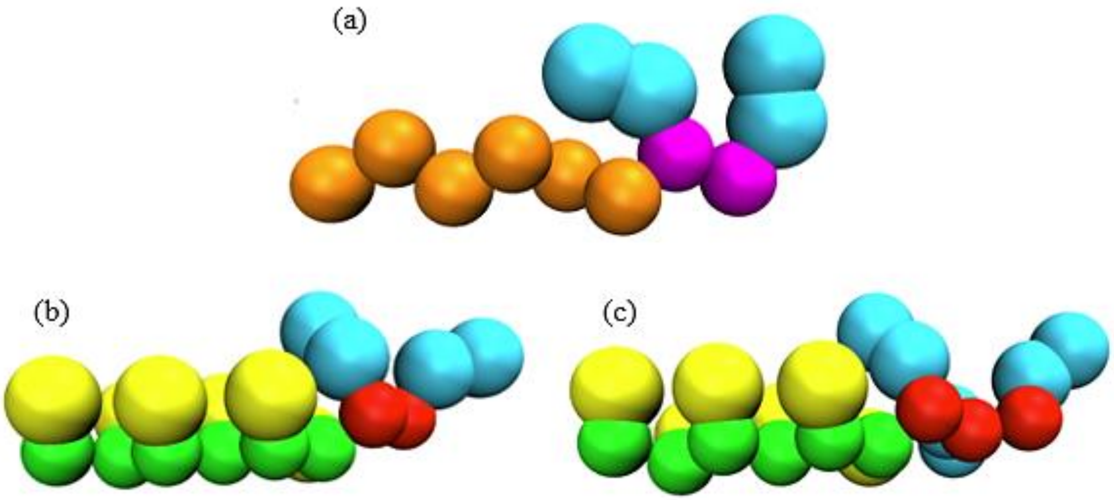

Figure 4.4. The MARTINI CG representations of the developed topologies for (a) A_6K_2, (b) V_6K_2, and (c) V_6K_3.

4.2.2 Simulation Parameters – A_6K and V_6K

The MARTINI CG Forcefield (v2.2p) was utilized to A_6K and V_6K models against the previous computational results[71]. To limit the degrees of freedom, both peptide models were capped at their N and C termini, resulting in a net +1 charge per peptide from the lysine residue to the systems. Chlorine (CL^-) ions were added to each system to counteract the charge on lysine and make the systems charge neutral. Simulations were built using the GROMACS software package (v5.1.4)[50-53]. 200 A_6K and V_6K peptides were randomly inserted into individual $(16\text{ nm})^3$ simulation boxes and solvated with 22801 and 22296 polarized water molecules, respectively. To remove particle overlaps due to the random insertion, the systems underwent energy minimization using the steepest descent integrator. After energy minimization the systems were equilibrated for 2000 ps to bring the box parameters to experimental values. Now ready for production, each of the two systems was run for a total of 10 μs.

Both simulations used the isothermal-isobaric ensemble (NPT). The A_6K simulation was run with a 25 fs timestep while the V_6K system, due to the presence of dihedrals, was run with a 10 fs timestep. Sun et al. use the Berendsen coupling methods[82] to maintain both temperature and pressure; this is generally frowned upon as the Berendsen methods do not accurately represent physical systems. The thermostat and barostat disfavor strong fluctuations in potential and kinetic energy by overdamping them, resulting in temperatures and pressures which deviate from the expected distribution[83]. Therefore, instead of the Berendsen methods, the velocity rescaling thermostat[54,55] and the Parrinello-Rahman barostat were used[56,57]. The temperature was maintained at 300 K with a coupling constant of 0.3 ps, and the pressure was maintained at 1 atm with a coupling constant of 5 ps as the 3 ps coupling constant was specific to the Berendsen parameterization and caused simulation failures during topology development. Electrostatic and van der Waals interactions were used in their shifted forms with a cutoff of 1.2 nm as per the normal MARTINI protocol. The neighbor list was updated every 10 steps with a distance cut-off of 1.4 nm.

4.2.2 Simulation Parameters – V_6K_2

The MARTINI CG Forcefield (v2.2p) was utilized to validate the V_6K_2 model against experimental results. To limit the degrees of freedom, V_6K_2 was capped at the N and C termini, resulting in a net +2 charge per peptide from the lysine residues to the system. Chlorine (CL^-) ions were added to each system to counteract the charge on lysine and make the systems charge neutral. Simulations were built using the GROMACS software package (v5.1.4)**[50-53]**. 200 V_6K_2 peptides were inserted into a $(11\ \mathrm{nm})^3$ simulation box using commands innate to GROMACS. The purely peptide system then underwent energy minimization using the steepest descent integrator to remove any overlaps caused by the random insertion. 8247 water molecules were then added to the system. Energy minimization was performed again using the steepest descent integrator. Equilibration was run for 500 ps, and once the system was ready for production, the simulation was run for 8 μs.

The simulation used the NPT ensemble and ran with a 10 fs timestep. The barostat and thermostat parameters are the same as those in Section 4.2.2 but the barostat coupling constant has been restored to 0.3 ps as no issues were encountered with its usage. Electrostatic and van der Waals interactions were used in their shifted forms with a cutoff of 1.2 nm as per the normal MARTINI protocol. The neighbor list was updated every 10 steps with a distance cut-off of 1.4 nm.

Due to the results obtained with the above protocol, a second system was developed to determine whether the computational expense of the polarizable water was necessary to the self-assembly pathways of the system or if comparable results could be achieved with standard water. MARTINI (v2.2) was used instead of MARTINI (v2.2p). 9106 standard water particles and 980 anti-freeze particles were added to the system as the new solvent. The temperature was raised from 300 K to 310 K to prevent the standard water from freezing and the coupling constant was lowered from 0.3 ps to 0.1 ps**[28]**. The coupling constant for the barostat was increased to 12 ps, and the compressibility was changed from $4.5e^{-5}$ to $3e^{-4}$ bar^{-1} as polarizable water is stiffer than standard water. The dielectric constant was increased to 15 for standard water. Besides the mentioned changes, the second system was run with the same parameters as the first.

4.3 A_6K and V_6K Model Validation

Sun et al. reported that, in their AA simulations, both A_6K and V_6K preferentially assemble themselves in anti-parallel arrangements during assembly, though V_6K has the potential to also assemble in a parallel configuration at a ratio of about 1:5[71]. These arrangements are clearly seen in Figure 4.5[71], which shows the final assemblies of their A_6K and V_6K CG simulations from three different views. In these assemblies, the backbone beads of both peptides are pink and the side chain beads of valine and lysine are shown in yellow and blue, respectively The A_6K peptides self-assembled into monolayer lamellas with an approximate thickness of 1.9 nm. The peptides which make up these monolayer lamellas appear to be arranged in an anti-parallel configuration with lysine side chains extending into the solvent on both sides of the monolayer lamella approximately equally. The clearest example of this is in the rightmost assembly view in Figure 4.5a. The V_6K peptides self-assembled into oblong, nanoplate-like assemblies, with diameters varying from 7.6 to 8.6 nm. The arrangement of the peptides in these assembles is less obvious: while the peptides mainly arrange themselves in an antiparallel configuration, there are sections of the assemblies in which the peptide side chains are arranged in a parallel configuration in a ratio of about 5:1. The diversity in alignment is clearest in the rightmost assembly view in Figure 5b.

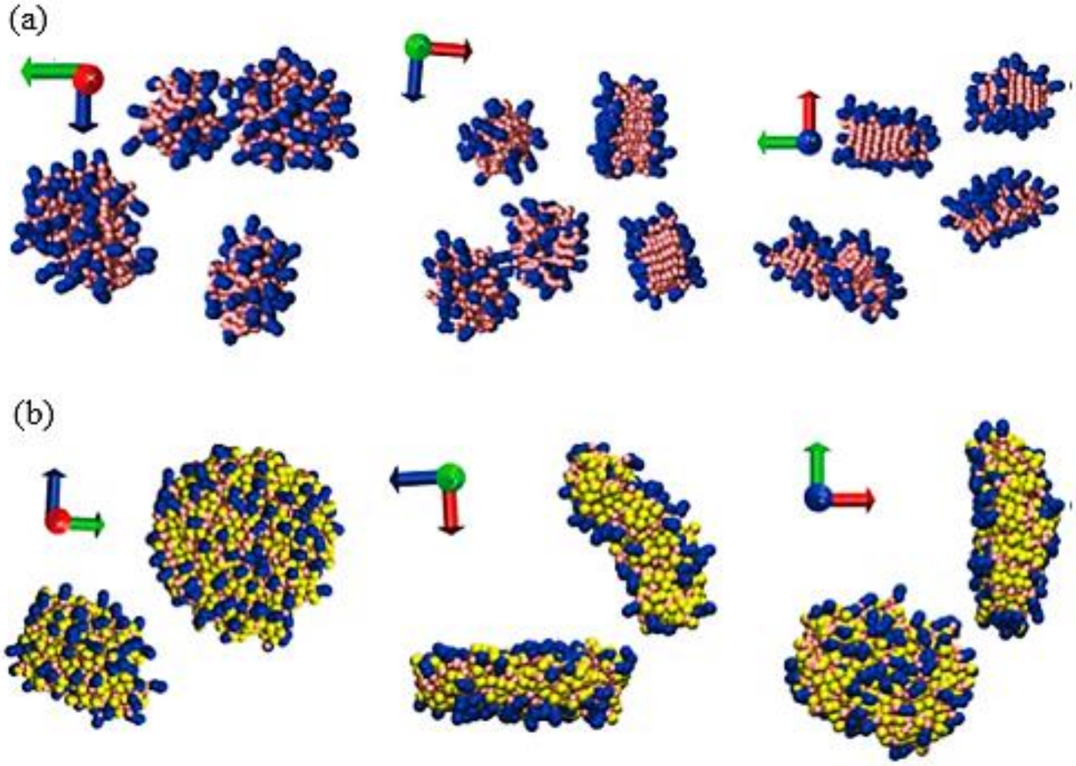

Figure 4.5. Final assembles from three different views for (a) A_6K and (b) V_6K. Alanine, valine, and lysine backbone beads are in pink, valine side chain beads are in yellow, and lysine side chain beads are in blue. (Reprinted with permission from Y. Sun, Z. Qian, C. Guo and G. Wei, *Biomacromolecules*, 2015, **16**, 2940–2949. Copyright © 2015, American Chemical Society.)

The results of the simulations containing the modeled peptides are found in Figure 4.6, with peptide bead type coloration matching that in Figure 4.2. The A_6K aggregates in Figure 4.6a appear to adopt the same anti-parallel configuration in monolayer lamellas that is shown in Figure 4.5a as indicated by the distribution of lysine on opposite sides of the aggregate. These lamellas have a comparable thickness to those previously reported. The V_6K aggregates in Figure 4.6b appear to resemble the nanoplate-like structures shown in Figure 4.5b. The uneven distribution of lysine on both sides of the aggregate indicates that the peptides form both parallel and anti-parallel alignments in the nanoplates. For convenience of comparison, Figure 4.7 contains three views of Figure 4.6 color-coded to match the color schemes used by Sun et al. in Figure 4.5.

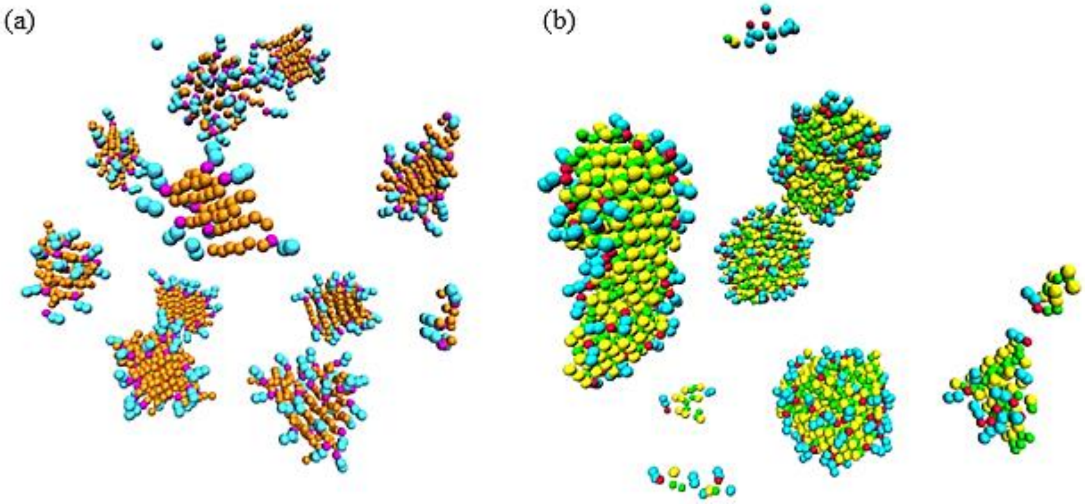

Figure 4.6. The final assemblies of the developed topologies for (a) A_6K and (b) V_6K. The pictures are colored based upon Figure 4.2.

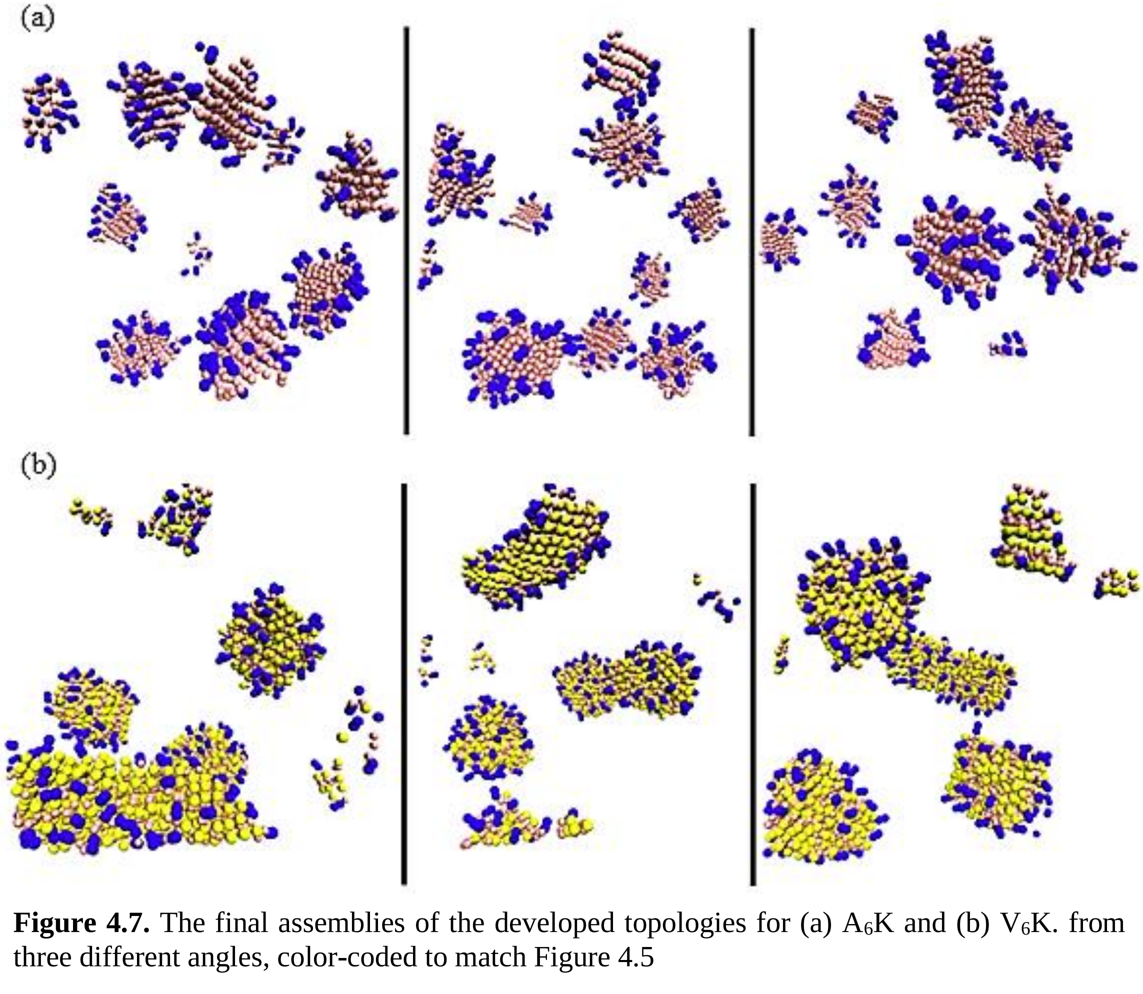

Figure 4.7. The final assemblies of the developed topologies for (a) A_6K and (b) V_6K. from three different angles, color-coded to match Figure 4.5

4.4 V_6K_2 Model Validation

4.4.1 Nanostructure Comparison

Once the developed V_6K model produced similar aggregates to those presented Sun et al.[71], a model for V_6K_2 was created. Unlike the A_6K and V_6K topology validation process, in which the alignment of the peptides as well as assemblies formed were considered, V_6K_2 topology validation was based upon comparison of how the model performed with regard to the reproduction of experimental results. V_6K_2 has been reported to experimentally self-assemble into nanotubes[65,68] and nanorods/nanofibers[67,84,85]. The classification difference between a nanotube and a nanorod is that a nanotube has a water core while a nanorod is solid throughout the structure.

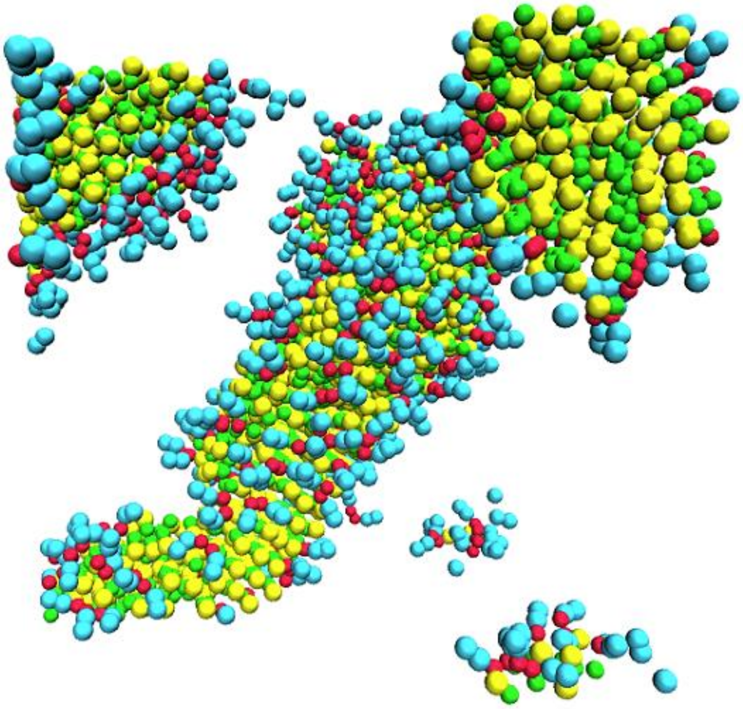

Figure 4.8. Self-assembled V_6K_2 nanorod parameterized by the developed topology. The nanorod stabilizes itself by interacting with itself through periodic boundaries. The colors are the same as those in Figure 4.2.

At a total peptide concentration of 0.162 peptides/nm^3, 200 V_6K_2 peptides, parameterized with a β-sheet secondary structure, self-assembled into a nanorod with a height of approximately 2 nm, a value which is within acceptable tolerances of the experimental results[84]. As shown in Figure 4.8, the nanorod stabilized as one aggregate by interacting with itself through periodic boundaries. The V_6K_2 peptides appear to arrange themselves much as the V_6K peptides did, with the majority in an anti-parallel configuration with some parallel arrangement.

4.4.2 Influence of Water Model on Nanostructure Organization

Once a successful nanostructure was achieved, the feasibility of the polarized water model in conjunction with V_6K_2 simulations was questioned. As previously mentioned in Chapter 2, polarizable water is much more computationally expensive to run than standard water by about a factor of three. It was chosen as the water model for the system as MARTINI polarizable water was specifically designed to work with polar substances[34]. However, the impact of polarizable water on the system versus the computational costs had not yet been qualitatively determined. To do so, a second V_6K_2 system was built where standard water and anti-freeze particles replaced polarizable water as the solvent. The total peptide concentration of the system was changed to 0.121 peptides/nm^3 by changing the size of the simulation box but keeping the number of peptides the same.

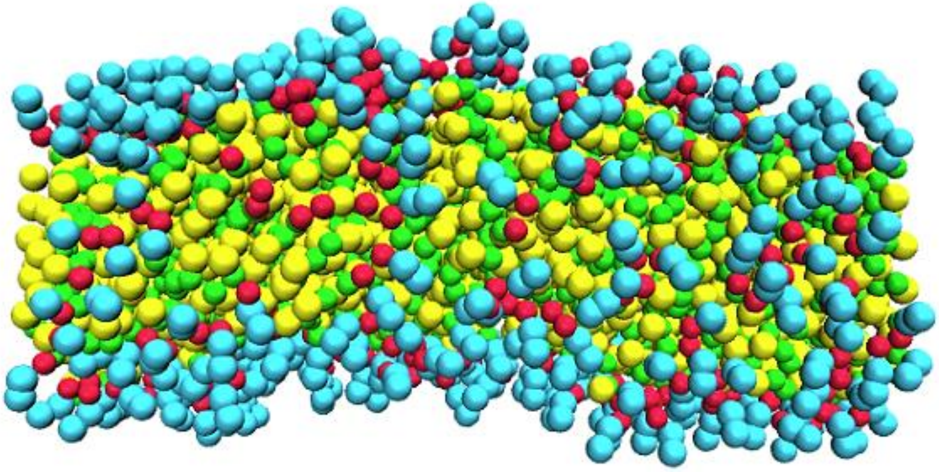

Figure 4.9. Self-assembled V_6K_2 nanorod parameterized by the developed topology. The nanorod stabilizes itself by interacting with itself through periodic boundaries. This nanorod was produced with standard water. The colors are the same as those in Figure 4.2.

The results for this system are found in Figure 4.9. Like the first system, the 200 V_6K_2 peptides self-assembled into a nanorod; however, the height of this nanorod is elliptical in nature with the larger height measured at 5.5 nm. The height differential is caused by how the V_6K_2 peptides arrange themselves in the nanostructure. In the nanorod in Figure 4.8, the alignment of the peptides is such that the width of the nanorod is never more than that of the peptides composing it. In the nanorod in Figure 4.9, however, the peptides appear to arrange themselves in a disorganized fashion, creating an elliptical cross-section. This difference is visualized in Figure 4.10. The implications of this phenomenon are currently under study.

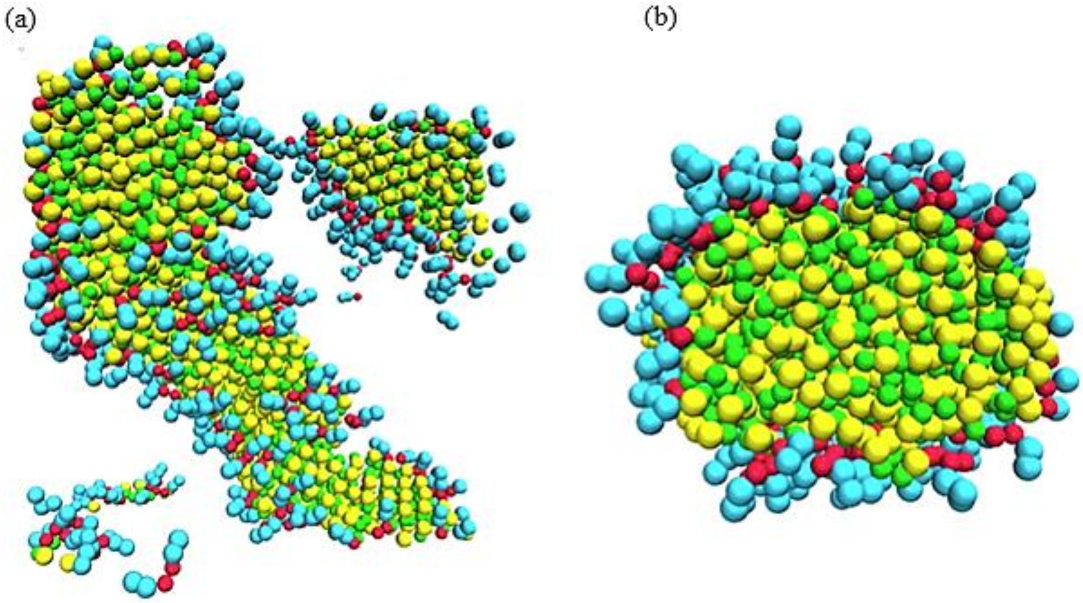

Figure 4.10. Comparison of the two V_6K_2 self-assembled nanorods formed by (a) polarizable water and (b) standard water. Both nanorods are have different dimensions and the peptides pack differently. The colors are the same as those in Figure 4.2.

4.5 Conclusions of the Aliphatic Peptide Study

Topologies for amphiphilic peptides A_6K and V_6K for use with the MARTNI CG framework were developed during this study. The results of CG simulations run with the developed models were validated through the comparison to the results of another computational study[71]. From the success with V_6K, a topology for one of its derivatives, V_6K_2, was created. This model was validated against experimental results, forming nanorods which matched the parameters of those previously reported.

The effect different types of MARTINI water had on the V_6K_2 assembly was examined through a comparison of the nanorods formed with polarizable water as a solvent versus standard water as a solvent. Results indicated that changing the solvent and therefore some of the system parameters changed how the V_6K_2 peptides arranged themselves: in polarizable water, they adopted uniform parallel and anti-parallel alignments while in standard water they arranged themselves elliptically. The reason as to why a change in water model results in a change in the assembly pathways is currently under study.

A manuscript is in preparation based upon computational studies performed with these molecular models.

Chapter 5

Future Directions

The projects discussed in Chapter 3 and Chapter 4 provide valuable insight into two classes of self-assembling peptides. The studies have laid the groundwork for the continuation of computational investigation into how peptide sequence variation impacts hybrid biological material characteristics. As more self-assembling peptides are translated for computational research, the breadth of research into biological materials which can be studied in conjunction with or even independently of experimental work will increase. This has positive implications for the medical field, but this enhanced research toolbox will also encourage and aid in the development of hybrid materials for use in other disciplines[86-88].

With regard to specific topologies, several avenues of research are available for the aliphatic peptide models of A_6K and V_6K, which have been validated against aggregates to determine peptide alignment. The A_6K and V_6K models can continue to be tested for the formation of supramolecular structures that are congruent with those formed in experiments. A_6K is reported experimentally to form long nanotubes[65-67, 68, 70, 77, 78-80, 89-91], though the reported conditions under which this can occur vary greatly. The experimental parameters that vary include solvent, pH, temperature, time before analysis performed, and whether the peptides are capped or uncapped. Results obtained with topologies which match those characterized in these papers provides a large phase space in which experimental results can be validated. V_6K is reported to either form just aggregates/stacks[67, 71, 80] or be insoluble in water[68]. A_6K_2 and V_6K_3 are both reported experimentally to self-assemble into vesicles[68]. Validation of the A_6K_2 and V_6K_3 models through results which agree with experimental outcomes would open avenues for further work with these peptides. Quantification of the packing of A_6K, V_6K, and V_6K_2 would further help solidify the models as being equivalent to experimental peptides.

Bibliography

1. B. Caughey and P. T. Lansbury, *Annual Review of Neuroscience*, 2003, **26**, 267–298.

2. C. Ke, M.-A. Sani, F. Ding, A. Kakinen, I. Javed, F. Separovic, T. P. Davis and R. Mezzenga, *Chemical Society Reviews*, 2017, **46**, 6492–6531.

3. M. Waqas, W.-J. Jeong, Y.-J. Lee, D.-H. Kim, C. Ryou and Y.-B. Lim, *Biomacromolecules*, 2017, **18**, 943–950.

4. T. Liu, P. Li, H. Jin, Q. Ding, Z. Zou and G. Peng, *Journal of Biomedical Materials Research Part A*, 2017, **105**, 2329–2334

5. C. Tang, X. Shao, B. Sun, W. Huang and X. Zhao, *International Journal of Molecular Sciences*, 2009, **10**, 2136–2145.

6. K. Mi, G. Wang, Z. Liu, Z. Feng, B. Huang and X. Zhao, *Macromolecular Bioscience,* 2009, **9**, 437–443.

7. C. M. B. Edwards, M. A. Cohen and S. R. Bloom, *Q.J.Med.*, 1999, **92**, 1–4.

8. M. E. Davis, P. C. H. Hsieh, T. Takahashi, Q. Song, S. Zhang, R. D. Kamm, A. J. Grodzinsky, P. Anversa and R. T. Lee, Proceedings of the National Academy of Sciences, 2006, 103, 8155–8160.

9. M. Wang, H. Adikane, J. Duhamel and P. Chen, *Biomaterials*, 2008, **29**, 1099–1108.

10. M. Wu, Z. Ye, Y. Liu, B. Liu and X. Zhao, *Molecular BioSystems*, 2011, **7**, 2040–2047.

11. R. Bansal and P. Kumar, Journal of Biomaterials Applications, 2017, 32, 40–53.

12. X. Yan, Q. He, K. Wang, L. Duan, Y. Cui and J. Li, *Angewandte Chemie International Edition*, 2007, **46**, 2431–2434.

13. F. Gelain, D. Bottai, A. Vescovi and S. Zhang, *PLoS ONE*, 2006, **1**, e119.

14. M. Zhou, A. M. Smith, A. K. Das, N. W. Hodson, R. F. Collins, R. V. Ulijn and J. E. Gough, *Biomaterials*, 2009, **30**, 2523–2530.

15. E. F. Banwell, E. S. Abelardo, D. J. Adams, M. A. Birchall, A. Corrigan, A. M. Donald, M. Kirkland, L. C. Serpell, M. F. Butler and D. N. Woolfson, *Nature Materials*, 2009, **8**, 596–600.

16. E. Kokkoli, A. Mardilovich, A. Wedekind, E. L. Rexeisen, A. Garg and J. A. Craig, *ChemInform*, 2007, **38**, 1015–1024.

17. V. N. Modepalli, A. L. Rodriguez, R. Li, S. Pavuluri, K. R. Nicholas, C. J. Barrow, D. R. Nisbet and R. J. Williams, *Biopolymers*, 2014, **102**, 197–205.

18. J. Liu, H. Song, L. Zhang, H. Xu and X. Zhao, *Macromolecular Bioscience*, 2010, **10**, 1164–1170.

19. A. Schneider, J. A. Garlick and C. Egles, PLoS ONE, 2008, 3, e1410.

20. S. Wan, S. Borland, S. M. Richardson, C. L. Merry, A. Saiani and J. E. Gough, *Acta Biomaterialia*, 2016, **46**, 29–40.

21. H. Song, L. Zhang and X. Zhao, *Macromolecular Bioscience*, 2010, **10**, 33–39.

22. K. Matsumoto, M. Vaughn, B. D. Bruce, S. Koutsopoulos and S. Zhang, *The Journal of Physical Chemistry B*, 2009, **113**, 75–83.

23. S. Koutsopoulos, L. Kaiser, H. M. Eriksson and S. Zhang, *Chem. Soc. Rev.*, 2012, **41**, 1721–1728.

24. K. Corin, P. Baaske, D. B. Ravel, J. Song, E. Brown, X. Wang, C. J. Wienken, M. Jerabek-Willemsen, S. Duhr, Y. Luo, D. Braun and S. Zhang, *PLoS ONE*, 2011, **6**.

25. R. N. Mitra, A. Shome, P. Paul and P. K. Das, *Org. Biomol. Chem.*, 2009, **7**, 94–102.

26. L. Lombardi, Y. Shi, A. Falanga, E. Galdiero, E. D. Alteriis, G. Franci, I. Chourpa, H. S. Azevedo and S. Galdiero, *Biomacromolecules*, 2019, **20**, 1362–1374.

27. L. Schnaider, S. Brahmachari, N. W. Schmidt, B. Mensa, S. Shaham-Niv, D. Bychenko, L. Adler-Abramovich, L. J. W. Shimon, S. Kolusheva, W. F. Degrado and E. Gazit, *Nature Communications*, 2017, **8**.

28. S. J. Marrink, H. J. Risselada, S. Yefimov, D. P. Tieleman and A. H. D. Vries, *The Journal of Physical Chemistry B*, 2007, **111**, 7812–7824.

29. C. A. López, A. J. Rzepiela, A. H. D. Vries, L. Dijkhuizen, P. H. Hünenberger and S. J. Marrink, *Journal of Chemical Theory and Computation*, 2009, **5**, 3195–3210.

30. J. J. Uusitalo, H. I. Ingólfsson, S. J. Marrink and I. Faustino, *Biophysical Journal*, 2017, **113**, 246–256.

31. J. J. Uusitalo, H. I. Ingólfsson, P. Akhshi, D. P. Tieleman and S. J. Marrink, *Journal of Chemical Theory and Computation*, 2015, **11**, 3932–3945.

32. L. Monticelli, S. K. Kandasamy, X. Periole, R. G. Larson, D. P. Tieleman and S.-J. Marrink, *Journal of Chemical Theory and Computation*, 2008, **4**, 819–834.

33. D. H. D. Jong, G. Singh, W. F. D. Bennett, C. Arnarez, T. A. Wassenaar, L. V. Schäfer, X. Periole, D. P. Tieleman and S. J. Marrink, *Journal of Chemical Theory and Computation*, 2012, **9**, 687–697.

34. S. O. Yesylevskyy, L. V. Schäfer, D. Sengupta and S. J. Marrink, *PLoS Computational Biology*, 2010, **6**.

35. J. N. Murrell and A. D. Jenkins, *Properties of liquids and solutions*, John Wiley & Sons, Chichester, 1997.

36. M. Reches and E. Gazit, *Science*, 2003, **300**, 625–627.

37. M. Reches and E. Gazit, *Israel Journal of Chemistry*, 2005, **45**, 363–371.

38. M. Reches and E. Gazit, *Current Nanoscience*, 2006, **2**, 105–111.

39. M. Reches and E. Gazit, *Journal of Nanoscience and Nanotechnology*, 2007, **7**, 2239–2245.

40. L. Adler-Abramovich and E. Gazit, *Journal of Peptide Science*, 2008, **14**, 217–223.

41. E. Gazit, *Chemical Society Reviews*, 2007, **36**, 1263–1269.

42. M. J. Krysmann, V. Castelletto, J. E. Mckendrick, L. A. Clifton, P. J. F. Harris, S. M. King and I. W. Hamley, *Langmuir*, 2008, **24**, 8158–8162.

43. R. Huang, R. Su, W. Qi, J. Zhao and Z. He, *Nanotechnology*, 2011, **22**, 245609.

44. P. W. J. M. Frederix, R. V. Ulijn, N. T. Hunt and T. Tuttle, *The Journal of Physical Chemistry Letters*, 2011, **2**, 2380–2384.

45. C. Guo, Y. Luo, R. Zhou and G. Wei, *ACS Nano*, 2012, **6**, 3907–3918.

46. A. N. Rissanou, E. Georgilis, E. Kasotakis, A. Mitraki and V. Harmandaris, *The Journal of Physical Chemistry B*, 2013, **117**, 3962–3975.

47. C. Guo, Z. A. Arnon, R. Qi, Q. Zhang, L. Adler-Abramovich, E. Gazit and G. Wei, *ACS Nano*, 2016, **10**, 8316–8324.

48. L. Adler-Abramovich, P. Marco, Z. A. Arnon, R. C. G. Creasey, T. C. T. Michaels, A. Levin, D. J. Scurr, C. J. Roberts, T. P. J. Knowles, S. J. B. Tendler and E. Gazit, *ACS Nano*, 2016, **10**, 7436–7442.

49. S. Mushnoori, K. Schmidt, V. Nanda and M. Dutt, *Organic & Biomolecular Chemistry*, 2018, **16**, 2499–2507. - Reproduced by permission of The Royal Society of Chemistry.

50. H. Berendsen, D. V. D. Spoel and R. V. Drunen, *Computer Physics Communications*, 1995, **91**, 43–56.

51. D. V. D. Spoel, E. E. Lindahl, B. Hess, G. Groenhof, A. Mark and H. Berendsen, *Journal of Computational Chemistry*, 2005, **26**, 1701–1718.

52. M. J. Abraham, T. Murtola, R. Schulz, S. Páll, J. C. Smith, B. Hess and E. Lindahl, *SoftwareX*, 2015, **1-2**, 19–25.

53. N. Goga, I. Marin, A. Vasilateanu, I.-B. Pavaloiu, K. O. Kadiri and O. Awodele, *2015 E-Health and Bioengineering Conference (EHB)*, 2015.

54. G. Bussi, D. Donadio and M. Parrinello, *The Journal of Chemical Physics*, 2007, **126**, 014101.

55. G. Bussi, T. Zykova-Timan and M. Parrinello, *The Journal of Chemical Physics*, 2009, **130**, 074101.

56. M. Parrinello and A. Rahman, *Physical Review Letters*, 1980, **45**, 1196–1199.

57. M. Parrinello and A. Rahman, *Journal of Applied Physics*, 1981, **52**, 7182–7190.

58. B. Hess, H. Bekker, H. J. C. Berendsen and J. G. E. M. Fraaije, *Journal of Computational Chemistry*, 1997, **18**, 1463–1472.

59. F. Aydin, P. Ludford and M. Dutt, *Soft Matter*, 2014, **10**, 6096–6108.

60. F. Aydin, G. Uppaladadium and M. Dutt, *The Journal of Physical Chemistry B*, 2015, **119**, 10207–10215.

61. F. Aydin, G. Uppaladadium and M. Dutt, *Colloids and Surfaces B: Biointerfaces*, 2015, **128**, 268–275.

62. J. N. Israelachvili, *Thermodynamic Principles of Self-Assembly.Intermolecular and Surface Forces*, 3rd edn, 2011, pp. 503–534.

63. Y. Song, S. R. Challa, C. J. Medforth, Y. Qiu, R. K. Watt, D. Peña, J. E. Miller, F. V. Swol and J. A. Shelnutt, *Chem. Commun.*, 2004, 1044–1045.

64. S. Vauthey, S. Santoso, H. Gong, N. Watson and S. Zhang, *Proceedings of the National Academy of Sciences*, 2002, **99**, 5355–5360.

65. G. V. Maltzahn, S. Vauthey, S. Santoso and S. Zhang, *Langmuir*, 2003, **19**, 4332–4337.

66. A. Nagai, Y. Nagai, H. Qu and S. Zhang, *Journal of Nanoscience and Nanotechnology*, 2007, **7**, 2246–2252.

67. Q. Wang, J. Yu, X. Zhang, D. Liu, J. Zheng, Y. Pan and Y. Lin, *RSC Advances*, 2013, **3**, 2784.

68. Q. Meng, Y. Kou, X. Ma, Y. Liang, L. Guo, C. Ni and K. Liu, *Langmuir*, 2012, **28**, 5017–5022.

69. G. Colherinhas and E. Fileti, *The Journal of Physical Chemistry C*, 2014, **118**, 9598–9603.

70. G. Colherinhas and E. Fileti, *The Journal of Physical Chemistry B*, 2014, **118**, 12215–12222.

71. Y. Sun, Z. Qian, C. Guo and G. Wei, *Biomacromolecules*, 2015, **16**, 2940–2949.

72. D. V. Waterhous and W. C. Johnson, *Biochemistry*, 1994, **33**, 2121–2128.

73. L. Ziserman, H.-Y. Lee, S. R. Raghavan, A. Mor and D. Danino, *Journal of the American Chemical Society*, 2011, **133**, 2511–2517.

74. F. Qiu, Y. Chen and X. Zhao, *Journal of Colloid and Interface Science*, 2009, **336**, 477–484.

75. F. Zhuang, K. Oglęcka and C. A. E. Hauser, *Membranes*, 2011, **1**, 314–326.

76. Y. Chen, C. Tang, Z. Xing, J. Zhang and F. Qiu, *Journal of Peptide Science*, 2013, **19**, 708–716.

77. H. Xu, J. Wang, S. Han, J. Wang, D. Yu, H. Zhang, D. Xia, X. Zhao, T. A. Waigh and J. R. Lu, *Langmuir*, 2009, **25**, 4115–4123.

78. J. Wang, S. Han, G. Meng, H. Xu, D. Xia, X. Zhao, R. Schweins and J. R. Lu, *Soft Matter*, 2009, **5**, 3870.

79. V. Castelletto, D. R. Nutt, I. W. Hamley, S. Bucak, Ç. Cenker and U. Olsson, *Chemical Communications*, 2010, **46**, 6270.

80. S. Han, W. Xu, C. Meiwen, W. Jiqian, D. Xia, H. Xu, X. Zhao and J. R. Lu, *Soft Matter*, 2012, **8**, 645–652.

81. Ç. Ç. Cenker, S. Bucak and U. Olsson, *Langmuir*, 2014, **30**, 10072–10079.

82. H. J. C. Berendsen, J. P. M. Postma, W. F. V. Gunsteren, A. Dinola and J. R. Haak, *The Journal of Chemical Physics*, 1984, **81**, 3684–3690.

83. S. Rogge, L. Vanduyfhuys, A. Ghysels, M. Waroquier, T. Verstraelen, G. Maurin and V. V. Speybroeck, *Journal of Chemical Theory and Computation*, 2015, **11**, 5583–5597.

84. M. K. Baumann, M. Textor and E. Reimhult, *Langmuir*, 2008, **24**, 7645–7647.

85. I. W. Hamley, *Soft Matter*, 2011, **7**, 4122.

86. J. Fan, L. Liu, S. Ding, M. Fu, F. Liu, C. Zhang, H. Wu, J. Wang and Y. Qin, *2016 IEEE International Nanoelectronics Conference (INEC)*, 2016.

87. R. A. Mansbach and A. L. Ferguson, *The Journal of Physical Chemistry B*, 2017, **121**, 1684–1706.

88. V. Nguyen, R. Zhu, K. Jenkins and R. Yang, *Nature Communications*, 2016, **7**, 13566.

89. U. Khoe, Y. Yang and S. Zhang, *Macromolecular Bioscience*, 2008, **8**, 1060–1067.

90. Ç. Ç. Cenker, S. Bucak and U. Olsson, *Soft Matter*, 2011, **7**, 4868.

91. Ç. Ç. Cenker, P. H. H. Bomans, H. Friedrich, B. Dedeoğlu, V. Aviyente, U. Olsson, N. A. J. M. Sommerdijk and S. Bucak, *Soft Matter*, 2012, **8**, 7463.